



City Research Online

City, University of London Institutional Repository

Citation: Stavropoulos Vasilakis, E., Rodriguez, C., Kyriazis, N., Malgarinos, I., Koukouvinis, P. & Gavaises, M. (2021). A direct forcing Immersed Boundary Method for Cavitating Flows. *International Journal for Numerical Methods in Fluids*, 93(10), pp. 3092-3130. doi: 10.1002/fld.5026

This is the accepted version of the paper.

This version of the publication may differ from the final published version.

Permanent repository link: <https://openaccess.city.ac.uk/id/eprint/26454/>

Link to published version: <https://doi.org/10.1002/fld.5026>

Copyright: City Research Online aims to make research outputs of City, University of London available to a wider audience. Copyright and Moral Rights remain with the author(s) and/or copyright holders. URLs from City Research Online may be freely distributed and linked to.

Reuse: Copies of full items can be used for personal research or study, educational, or not-for-profit purposes without prior permission or charge. Provided that the authors, title and full bibliographic details are credited, a hyperlink and/or URL is given for the original metadata page and the content is not changed in any way.

City Research Online:

<http://openaccess.city.ac.uk/>

publications@city.ac.uk

A direct forcing Immersed Boundary Method for Cavitating Flows ^{*}

E. Stavropoulos Vasilakis[†], C. Rodriguez; N. Kyriazis; I. Malgarinos; P. Koukouvinis; M. Gavaises
School of Mathematics, Computer Science and Engineering, CITY, University of London, UK

July 15, 2021

Abstract

In the current study, an Immersed Boundary Method for simulating cavitating flows with complex or moving boundaries is presented, which follows the discrete direct forcing approach. Although the Immersed Boundary Methods are widely used in various applications of single phase, multiphase and particulate flows, either incompressible or compressible, and numerous alternative formulations exist, to the best of the authors' knowledge, a handful of computational works employ such methodologies on cavitating flows. The herein proposed method, following the works of the author's group [1–3], tries to fill this gap and to solidify the development of a computational tool of a simple formulation capable to tackle complex numerical problems of cavitation modelling. The method aims to be used in a wide range of applications of industrial interest and treat flows of engineering scales. Therefore, a validation of the method is performed by numerous benchmark test-cases, of progressively increasing complexity, from incompressible low Reynolds number to compressible and highly turbulent cavitating flows.

1 Introduction

Within the framework of Computational Fluid Dynamics, applications of industrial interest often refer to flows in complex geometries or around moving bodies; their simulation may be numerically challenging and computationally expensive. Many cases of cavitating flows fall into that category. For example, cavitation formation in Diesel injector nozzles with moving needle, gear pumps or propellers mounted under ship hauls, refer to problems with moving geometrical parts and include different geometrical features with wide range of length scales and topological features that impose severe constraints in mesh generation. The conventional strategy of generation of boundary-conforming grids for such problems, may become demanding and time consuming. When the numerical simulation involves moving parts with large displacements, common conformal grid strategies result in re-meshing of the entire domain in every time-step [4], or deforming the grid and adding or removing cell-layers when a desired cell size is reached [5]. In the case of marine propellers, to accommodate their rotational motion, either the entire computational domain would be rotated accordingly [6], or a multi-region mesh would be used, which lets the part of the grid that conforms with the propeller blades to slide with regards to the global domain [7]. Another approach of over-set grids [8] (also known as Chimera grids), employs multiple overlapping grids, each one handling a separate geometrical feature, and relies on interpolating the solution between them. These techniques increase significantly the difficulty of the simulations and their computational cost.

Immersed Boundary Methods [9] offer a remedy to these computational obstacles, allowing modelling arbitrary complex and moving or deforming bodies on a simple non-conformal grid. The presence of immersed boundaries is modelled through alternations of the governing equations which are solved on a simple canonical Cartesian grid. Thus, Immersed Boundary Methods simplify the grid generation and ease the complex geometry manipulation, resulting in smoother and higher-quality grids that decrease the computational load. Especially in problems where moving boundaries are present, the computational cost would drop significantly and the results' quality would increase, because the overall computational domain would not be modified, but instead the influence of the moving body would be relocated to new cells.

The Immersed Boundary Method was first introduced by Peskin [10], who studied the incompressible blood flow inside the heart, by solving the flow equations on a Cartesian non-conformal mesh and adding a force term in the momentum equations representing the elastic boundaries of the heart, immersed in the global computational domain. According to studies of Mittal and Iaccarino [9] and Iaccarino and Verzicco [11], the Immersed Boundaries Methods can be classified into *indirect* boundary condition imposition methods, which include *continuous* or *discrete* forcing and *penalization* approach, and *direct* boundary condition imposition methods, which refer to *ghost-cell* or *cut-cell* formulations. A similar classification is followed by Sotiropoulos and Yang [12], where the methods are divided into *diffused interface*, corresponding to *indirect* methods, and *sharp interface*, corresponding to *direct* methods.

In the indirect methods, the *no-slip* boundary condition at the immersed body surfaces is imposed not by setting the boundary value but rather by introducing a forcing term in the momentum equation that drives the solution to the desired value. The forcing term can be added in to the continuous form of the equations (*continuous forcing*) or can be introduced after the discretisation (*discrete forcing*). The method developed by Peskin [10] falls in the continuous

^{*}This is the peer reviewed version of the following article: "Stavropoulos Vasilakis, E., Rodriguez, C., Kyriazis, N., Malgarinos, I., Koukouvinis, P. and Gavaises, M. (2021), *A direct forcing Immersed Boundary Method for Cavitating Flows*. Int J Numer Meth Fluids. Accepted Author Manuscript", which has been published in final form at <https://doi.org/10.1002/flid.5026>. This article may be used for non-commercial purposes in accordance with Wiley Terms and Conditions for Use of Self-Archived Versions.

[†]Corresponding Author: evangelos.stavropoulos-vasilakis.5@city.ac.uk

approach category and addressed problems of elastic boundaries. In the case of rigid boundaries however, the continuous forcing approach may result in stiff algebraic systems or lead to stability problems for highly unsteady flows [9], as it would require very large values of modulus of elasticity [13] or an iterative feedback forcing technique with high values of damping coefficients [14]. On the other hand, the discrete forcing approach, overcomes these issues for rigid bodies, by usually employing an initial prediction step where the momentum equations are solved, neglecting the forcing term; the estimated velocity is used to evaluate the forcing term [15–19]. In addition, although the majority of the aforementioned IB methodologies are developed for incompressible flows and incorporated in pressure-correction algorithms, recently a discrete forcing IB method was proposed for compressible flows, enforcing a pressure boundary condition on the IB body through a source term [20].

In the direct methods, the desired *wall* boundary conditions (*b.c.*) for the immersed body are imposed by alternations in the numerical stencil on the computational cells in the vicinity of the interface between the fluid and solid domains, defined by the immersed body. According to the *ghost-cell* approach [21–25], boundary conditions are imposed on cell faces and nodes in the immediate vicinity of the immersed interface. The *b.c.* values are calculated by means of interpolation between the *ghost* *b.c.* points and their projection on the immersed interface, with the use of artificial mirror points, in order for the wall *b.c.* to be satisfied on the interface. On the contrary, the *cut-cell* methods [26, 27] reconstruct the immersed boundary by altering the geometry and the topology of the computational cells cut by the immersed interface. The computational cells are divided into fluid and solid sub-cells by the intersecting immersed surface, which creates new faces in the cells upon which the boundary conditions are applied. The computational cells’ topology therefore is altered; for instance regular hexahedral cells may become generic polyhedral and thus, the equations’ discretisation is modified. These methods are considered to provide the most mathematically and geometrically accurate representation of the immersed body.

Immersed Boundary Methods have been used to cover a wide range of applications and flow regimes. Examples include (but are not limited to) the work of Borazjani et al. [21–23], who used a ghost-cell approach to simulate the moderate Reynolds ($Re \simeq 6000$) flow through mechanical heart valves; Luo et al. [24] utilized a ghost-cell method in cases of incompressible flows with heat-exchange; Uhlmann [17] employed a direct forcing approach on incompressible flows with particles; Municchi and Radl [28, 29] studied momentum, heat and mass transfer of gas-particle suspensions with a hybrid of direct forcing and Fictitious Domain (*FD*) methods; discrete forcing methods were applied by Blais et al. [18] on incompressible viscous mixing and by Mochel et al. [19] on compressible high Re flow around a space launcher, using Zonal Detached-Eddy simulations (ZDES); Fadlun et al. [16] and Cristallo and Verzicco [30] made use of direct forcing IB methods to perform Large Eddy Simulation (LES) of the high Reynolds flow in an Internal Combustion (*IC*) engine’s cylinder with a moving piston; Arienti et al. [31] studied the incompressible flow through a Diesel injector nozzle, with the aid of a level-set cut-cell Cartesian grid solver; Pasquariello et al. [27] combined a compressible cut-cell fluid solver with a finite-element structural solver to study Fluid Structure Interaction (FSI) problems of shock wave interactions with deformable thin structures. However, to the best of the authors’ knowledge, a handful of computational works employ IB approaches on cavitating flows.

Battistoni et al. [32], Zhao et al. [33] as well as Örley et al. [34–36] employed cut-cell IB methodologies on the numerical study of cavitation inception in Diesel injectors with moving needle. The recent works of Huang et al. [37] and Lee et al. [38] on cavitation induced by the motion of underwater projectiles, and Xu et al. [39, 40] on cloud cavitation around blunt bodies followed a cut-cell approach as well. On the other hand, a direct forcing method has been chosen by the authors’ group to study cavitation induction in Diesel injectors (Mithun et al. [41]), in gear pumps (Mithun et al. [3]) and during the closure of the claw of the pistol shrimp (Koukouvinis et al. [1]). The authors also presented in a previous article [2] a study of shock-wave generation and the induced cavitation by the high-velocity impact (Mach=0.7) of a solid projectile on a water jet; in this work, the projectile was modelled via a similar formulation of the direct forcing Immersed Boundary approach proposed herein.

The approach presented herein falls in the category of *direct forcing* methods [9, 11], as the presence of the boundary is taken into account by introducing a volumetric source term in the momentum equations. The forcing is localised on cells completely or partially covered by the immersed body, using a continuous color function expressing the cells’ coverage. The forcing term’s formulation is similar to the one found in the works [1–3]; however the integration of the source term to the computational algorithm differs.

The forcing methods usually involve Lagrangian-Eulerian transformations, because the forcing term is first evaluated on the Lagrangian points that represent the immersed boundary and then spread on the neighbouring Eulerian computational cells using a Dirac delta function. The Lagrangian-Eulerian and the inverse transformations could become the bottle-neck of the numerical solution of the governing equations. Discrete forcing Immersed Boundary methods [18, 19] that evaluate the forcing term in the Eulerian frame and apply it to all the cells of the immersed body region, by-pass this issue. In addition, ghost-cell approaches require a large number of interpolations that can be a drawback of the computations [29]. Considering that high order of accuracy requires more layers of *ghost-cells* [24] or finer resolution of the solid surface [29], the computational burden of the interpolation procedure becomes not negligible when employing four point interpolation stencils for each point discretising the immersed solid surface [24]. Moreover, in ghost-cell or some forcing methodologies, the projection of the immersed boundary on the background mesh may result in a *stair-case* representation of the body as the partially covered cells are not considered as solid cells; in the case of moving immersed bodies, where the immersed surface gradually covers the computational cells but the cells are abruptly removed or re-introduced in the fluid sub-domain, this can lead to spurious oscillations in the solutions. This issue is overcome by the cut-cell methods, or by forcing methods considering even the partially covered cells. However, cut-cell methods involve complex and computationally expensive geometrical and topological manipulations. The computational cost of identify-

ing intersections of the IB geometry, represented by M triangles, with the computational cells, on a $N \times N \times N$ mesh, and creating the *cut-cells* is estimated at the order of $\mathcal{O}(N^2 \cdot M \cdot \log M)$ (for tree-based data structure) [42]. Also, *cut-cell* methods usually result in very small computational cells of arbitrary shape and thus, suffer from *small cell stability problem*; *cell-merging* and *cell-linking* [26, 43] or *flux redistribution* [44, 45] or a combination of both approaches coupled with detailed reconstruction of the intersection using triangulation of the cut-faces [35] can be performed to remove the problematic small cells. This may also constrain computations and prohibit the full closure of small clearances and solid-to-solid contact; for instance when modelling the closure of a needle valve, a minimum gap between the immersed boundary and the solid wall of at least one computational cell may be a strict requirement [32–34]. Therefore, it becomes apparent that the use of a *direct forcing* Immersed Boundary approach for cavitating flows can offer advantages.

The aim of the current work is to propose a direct forcing IB methodology, assess its performance and demonstrate its applicability on a wide range of applications of industrial interest. Moreover, with regards to the ghost-cell and other direct forcing methods, it avoids the cumbersome Lagrangian-Eulerian interpolation, and overcomes the stair-case problem by using a continuous mask that localises the forcing term on all the fully and partially covered by the immersed body cells. The assessment of the method is performed in various flow regimes, from incompressible laminar and low-Reynolds flows ($Re = 100$) to high-Reynolds turbulent multiphase flows ($Re = 10^6$), to compressible flows with or without cavitation, and considering either stationary or moving boundaries; the computational results are compared against experimental data whenever available or against prior numerical simulations.

The method is developed within the open-source software platform of *OpenFOAM* [46]. It is designed to take advantage of the wide variety of the available computational features or tools, as well as to be independent of the discretisation of the equations and able to be integrated in different solvers and solution algorithms. The *portability* of the method is demonstrated by the fact that the forcing method can be coupled, in one hand with an explicit density based solver, developed in-house, as presented by the authors in a previous work [2] and further discussed hereafter, and on the other hand with a standard implicit pressure based solver, distributed with OpenFOAM, as presented herein.

In the following sections of the paper the numerical methodology is initially presented, followed by its thorough validation against well documented benchmark cases. First, the method is tested on the simple laminar incompressible cases of a moving cylinder in stationary liquid and a moving cylinder in free stream. Next, the turbulent incompressible flow over a back-facing step and the low-Reynolds but high Mach compressible flow past a stationary cylinder are simulated. Then, the method is applied on the simulation of cavitating cases, initially to the cavitation induction by the rotation of a cross in stagnant water, then to the turbulent cavitating flow past a stationary hydrofoil in a cavitation tunnel and subsequently on the case of turbulent cavitating flow over a pitching hydrofoil. Finally the application of the method on a demanding problem of engineering scales, that of cavitation inception in Diesel injector, is presented. The most important conclusions are summarised at the end.

2 Methodology

The proposed Immersed Boundary method, follows a direct forcing approach [9, 11] that introduces a volumetric source term in the discretised Navier-Stokes equations, which are solved using an operator-splitting algorithm.

2.1 Governing equations

The Reynolds Averaged Navier-Stokes (RANS) approach is adopted and the governing equations for the Newtonian fluids, in their general compressible form, are given by 2.1; the vectors are denoted with bold font.

$$\frac{\partial \rho}{\partial t} + \nabla \cdot \rho \bar{\mathbf{u}} = 0 \quad (2.1a)$$

$$\frac{\partial \rho \bar{\mathbf{u}}}{\partial t} + \nabla \cdot (\rho \bar{\mathbf{u}} \bar{\mathbf{u}}) = -\nabla p - \nabla \cdot (\bar{\boldsymbol{\tau}} + \boldsymbol{\tau}_R) + \mathbf{f}_{Ib} \quad (2.1b)$$

The immersed boundary is modelled through the addition of the volumetric source term \mathbf{f}_{Ib} in the momentum equation 2.1b; its formulation is discussed in the following section. For the solution of the governing equations, two different numerical approaches are utilised: the pressure-based and the density-based, within the framework of OpenFOAM [46]. Both methodologies follow the Homogeneous Equilibrium Model (*HEM*) [47] to consider the presence of cavitation. This considers both mechanical and thermal equilibrium when two or more different fluids are present; their mixture is seen as a "pseudo-fluid" with average properties governed by a single set of conservation equations.

In addition, in both implementations, the phase-change is modelled through the barotropic law. The current study treats primevally cases of hydrodynamic cavitation, where flow is often treated as isothermal [4, 48, 49]; however, the assumption that thermal effects play a role is followed even in cases of cavitating flows inside Diesel injector nozzles [5, 36, 50, 51].

2.1.1 Pressure-based solver

The *cavitatingFoam* solver of OpenFOAM is used, which is a compressible pressure-based solver, employing HEM and following an iterative pressure correction algorithm. The mixture composition, and therefore its density and viscosity, is

function of the vapour volume fraction α_v , which is calculated by equation 2.2.

$$\alpha_v = \frac{\rho - \rho_{v,sat}}{\rho_{l,sat} - \rho_{v,sat}}, \quad \rho < \rho_{l,sat} \quad (2.2)$$

Thermal effects are neglected, therefore the energy equation is not solved and the closure of the differential system of equations 2.1 is provided by an Equation of State (*EOS*) linking the density directly to pressure 2.3 using the compressibility of the mixture ψ . From the different models available for the calculation of the ψ , the Wallis model is chosen, which is expressed by the formula 2.3b. The compressibility of each phase is calculated as the inverse of the speed of sound squared $1/c^2$.

$$\rho = \psi p + (1 - \alpha_v)\rho_{L,0} - ((\alpha_v\psi_v + (1 - \alpha_v)\psi_l) - \psi)p_{sat} \quad (2.3a)$$

$$\psi = (\alpha_v\rho_{v,sat} + (1 - \alpha_v)\rho_{l,sat}) \cdot \left(\frac{\alpha_v\psi_v}{\rho_{v,sat}} + \frac{(1 - \alpha_v)\psi_l}{\rho_{l,sat}} \right) \quad (2.3b)$$

Within the framework of OpenFOAM [46], pressure-based solvers, both incompressible and compressible, widely use an iterative pressure-correction algorithm called PIMPLE [52]. The PIMPLE algorithm is a combination of the Pressure Implicit with Splitting of Operators (*PISO*) [53] and the Semi-Implicit Method for Pressure Linked Equations (*SIMPLE*) [54] algorithms. It can be seen as an iterative PISO algorithm, which searches for a steady-state solution in each time step using under-relaxation, and therefore allows the use of larger time-steps than PISO.

Introducing the barotropic EOS into the continuity equation 2.1a, the pressure-correction equation 2.4 is extracted. The algorithm, in every (outer) iteration, solves the momentum equation 2.1b, then performs pressure-correction via 2.4 in the PISO loop and then updates ρ , α_v and ψ by 2.3a, 2.2 and 2.3b respectively, until convergence is reached.

$$\frac{\partial\psi p}{\partial t} - (\rho_{l,0} + (\psi_l - \psi_v)p_{sat}) \frac{\partial\alpha_v}{\partial t} - \frac{\partial\psi}{\partial t} p_{sat} + \nabla \cdot \rho \mathbf{u} = 0 \quad (2.4)$$

2.1.2 Density-based solver

A density-based solver, noted as `2phaseFoam`, has been developed by the authors' research team [55] within OpenFOAM; its inviscid formulation has been coupled with the immersed boundary methodology presented herein to simulate the solid projectile's impact on water jet [2].

This solver is also based on the HEM approach, but considers the presence of liquid, vapour and immiscible gas and two different mixtures: one mixture of liquid and its vapour, and one mixture of the liquid-vapour system and the gas. The liquid-vapour system obeys the linear barotropic EOS, while the gas follows the isothermal ideal gas EOS. The energy equation is not considered, since the isothermal assumption is adopted.

The differential system of equations 2.1 is solved using the mixture's properties and an advection equation is used for the immiscible gas' mass fraction Y_g 2.5a; surface tension effects are neglected. The mixture's density is calculated as function of the volume fractions of the liquid-vapour mixture β_{lm} , vapour α_v and gas β_g , by equation 2.5b, while the viscosity will be discussed in a following section. For the volume and the mass fractions, β_i , Y_i respectively, of the components, relations 2.5c hold true and therefore the local vapour volume fraction is given by the slightly altered expression 2.5d. The density of the liquid-vapour mixture is calculated by equation 2.6a and that of the gas by equation 2.6b, as functions of the speed of sound c_i . For the immiscible isothermal gas, the speed of sound is estimated by the ideal gas EOS, $c_g = \sqrt{R_g T_{ref}}$, based on the specific gas constant and a reference temperature. For the liquid-vapour mixture, the speed of sound c_{lm} is determined by the Wallis relation for the three-phase mixture 2.6c. Equations 2.6a and 2.6b, combined with 2.5b and 2.5c, are used to derive an equation for the calculation of the mixture's pressure and close the system; the resulting equation is of quadratic form and is solved iteratively so as its roots fulfil the original assumptions. For more details the reader is referred to the original work of Kyriazis et al. [55].

$$\frac{\partial\rho Y_g}{\partial t} + \nabla(\rho \mathbf{u} Y_g) = 0 \quad (2.5a)$$

$$\rho = \beta_{lm}((1 - \alpha_v)\rho_l + \alpha_v\rho_v) + \beta_g\rho_g \quad (2.5b)$$

$$\beta_i = \frac{v_i}{V}, \quad \sum_i \beta_i = 1 \quad \text{and} \quad Y_i = \frac{m_i}{m}, \quad \sum_i Y_i = 1 \quad \text{and} \quad \rho_i = \frac{Y_i}{\beta_i} \quad (2.5c)$$

$$\alpha_v = \beta_{lm} \cdot \frac{\rho - \rho_{v,sat}}{\rho_{l,sat} - \rho_{v,sat}}, \quad \rho < \rho_{l,sat} \quad (2.5d)$$

$$\rho_{lm} = \rho_{l,sat} + \frac{1}{c^2}(p - p_{sat}), \quad c = \begin{cases} c_l, & p \geq p_{sat} \\ c_{lm}, & p < p_{sat} \end{cases} \quad (2.6a)$$

$$\rho_g = \frac{p}{c_g^2} = \frac{p}{R_g T_{ref}} \quad (2.6b)$$

$$\frac{1}{\rho c^2} = \frac{1 - \beta_g}{\rho_{lm} c_{lm}^2} + \frac{\beta_g}{\rho_g c_g^2} \quad (2.6c)$$

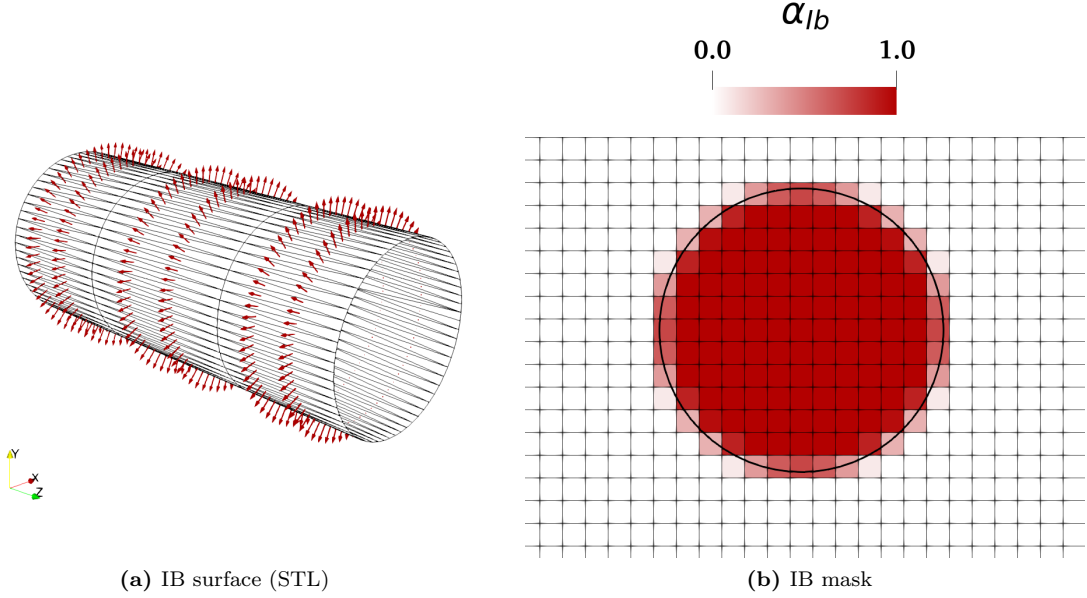


Figure 1: Representation of immersed boundary by a triangulated surface, with the equivalent surface normals, (left) and its projection onto the computational grid through the IB *mask* α_{Ib} (right).

2.1.3 Numerical Schemes

The discretisation of the equations in time and space, for the proposed methodology can be generic. With regards to the implicit pressure-based approach, for the laminar incompressible cases, the 1st order accurate Euler time scheme has proven adequate, but for the turbulent or cavitating cases, the 2nd order Crank-Nicolson scheme is more appropriate. In a similar way, for the laminar incompressible cases *Gauss upwind* 1st order accurate scheme is used, while for the more complicated cases 2nd order spatial schemes are employed.

On the other hand, the density-based solver, employs an explicit four stage Runge-Kutta (RK_4) time-advancement, 4th order accurate in time. It also makes use of special hybrid flux, to tackle issues arising from the great variations of speed of sound in compressible three-phase mixtures. The hybrid flux is based on Primitive Variable Riemann Solver and Mach consistent flux [55, 56].

The time step in the simulations is controlled by the Courant-Friedrichs-Lewy (CFL) condition:

$$Co = \max(\Delta t \cdot \sum_{faces} |\phi_i| / 2V) \leq 0.5 \text{ or } 1$$

For the cavitating flows, an additional constraint is added, due to the variation of the Mach number in the liquid and vapor phases, which is expressed by the *acoustic* Courant number, defined as:

$$Co_{ac} = \max\left(\Delta t / \left(2V\sqrt{\psi}\right)\right) \leq 1 \text{ or } 2$$

2.2 The IB forcing formulation

The immersed solid boundary is represented by a surface mesh; a color function is used to indicate the *solid* or the *IB cells* and the computational grid cells enclosed by this surface. Figure 1 presents the triangulate surface of a cylinder and the equivalent projection through the color function on the computational domain.

The default octree-search algorithm of OpenFOAM is used to initially find the grid cells with the cell centre lying inside the IB shell; then the *solid stencil* is extended to include the grid cells cut by the IB surface. The color function (*IB mask*) representing the solid area, corresponds to the *solid volume fraction* of the cells. This function receives values *continuously* between 0 for *fluid cells* and 1 for *solid cells*; cells with intermediate values correspond to the interface between the solid and the fluid area. For each computational cell, the mask is calculated as the average of the normal distance of all the vertices of the cell from the IB surface [1]. For each computational cell, the *singed* distance of each of its vertices from the nearest IB surface point is estimated, as seen in figure 2a, with negative distance indicating a vertex in the solid region. Then the sum of the distance of the vertices inside the solid region is divided by the sum of the distance of all the vertices; this is expressed by the relation 2.7 for each of the N_c cells with N_v vertices.

$$\alpha_j = \frac{\sum_{i=1}^{N_v} | \min(d_{n,ij}, 0) |}{\sum_{i=1}^{N_v} | d_{n,ij} |}, \quad j \in [1, N_c] \quad (2.7)$$

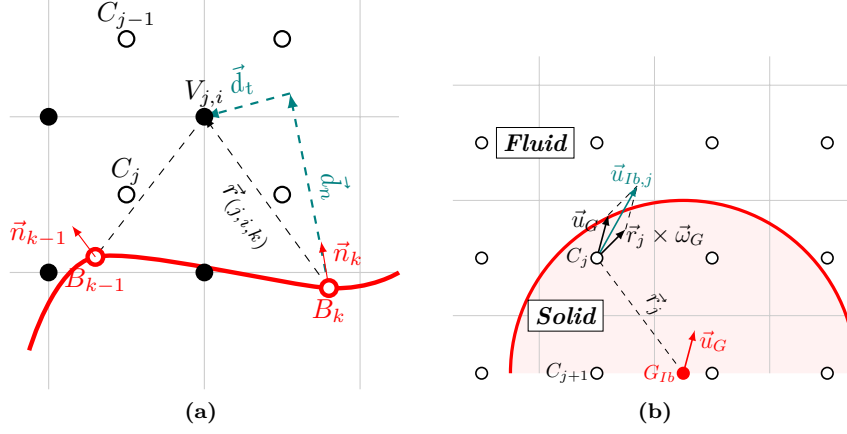


Figure 2: Calculation of the distance of each grid node from the IB surface (*left*) and of the *target* velocity for each cell in the IB region (*right*).

The forcing source term, seen in 2.8, is calculated as the difference of the fluid velocity from the IB solid velocity divided by the time step. By multiplying with the IB mask, the source term is localised on all the cells in the IB region and not only on the interface. The term is designed to drive the solution of the equation to the desired velocity value in the IB region, imposing a no-slip condition on the IB cells. The *targeted* velocity value to be imposed in each computational cell in the IB region is calculated with respect to the centre of gravity of the IB surface taking into account the rotation of the body, as $\mathbf{u}_{Ib,j} = \mathbf{u}_G + \mathbf{r}_j \times \omega_G$; this procedure is visualised in figure 2b.

$$\mathbf{f}_{Ib} = \alpha_{Ib} \cdot \frac{\mathbf{u}_{Ib} - \mathbf{u}_{fluid}}{\Delta t}, \quad \alpha_{Ib} \in [0, 1] \quad (2.8)$$

When the IB methodology is combined with a pressure-correction algorithm, the forcing term is updated in every pressure-correction iteration. In this way, although the forcing term expression has an explicit formulation using the previously estimated velocity field, it is treated implicitly as it is updated throughout the iterations of the time step, following the evolution of the velocity field. With respect to the implementation used by the authors' group in previous works [1, 3], within the framework of commercial CFD software, the use of case-dependant arbitrary forcing amplification coefficient is avoided.

If this forcing term is formulated explicitly, using the velocity value of the previous time-step or iteration, can receive large values, which can lead to very stiff matrices. This holds true especially for the cavitating flows, when the time-step tends to reach values of $10^{-7} \sim 10^{-8}s$, limited by high velocities or large deviation of the Mach number between the liquid, vapour and mixture. In order to tackle this difficulty, the IB source term can be treated implicitly by being linearised [57, 58], following Taylor expansion, as:

$$f_{Ib,k}(u_k)^t = f_{Ib,k}(u_k)^{t-1} + \frac{\partial f_{Ib,k}}{\partial u_k} \cdot (u_k^t - u_k^{t-1}), \quad k = x, y, z$$

with regards to the time step t . When the IB methodology is combined with a pressure-correction algorithm, the forcing term should be updated in every pressure-correction iteration. Therefore for every intermediate step n within each time step t , the forcing term is calculated by 2.9:

$$f_{Ib,k}(u_k)^n = f_{Ib,k}(u_k)^{t-1} + \frac{\partial f_{Ib,k}}{\partial u_k} \cdot (u_k^n - u_k^{t-1}), \quad k = x, y, z \quad (2.9)$$

When the IB methodology is combined with the explicit density-based algorithm, the forcing term is updated once at the beginning of the time-step and then it is integrated as part of the momentum equation according to the RK4 scheme.

2.3 Turbulence modelling

Within the framework of RANS simulations, the treatment of turbulent flows reduces to the computation of the Reynolds stresses tensor τ_R in 2.1b. Regular turbulence models can be used in conjunction with the proposed Immersed Boundary Method, with slight modifications. As discussed by Balaras [59] and Cristallo et Verzicco [30], within the framework of LES, and by Mochel et al. [19], within the framework of RANS, the boundary condition of the turbulent variable should be applied in the region or the interface of the immersed boundary and thus, the models should be adjusted.

Firstly, a source term is added to the transport equations of the turbulent variables, in a similar form of 2.8, in order to drive the solving variable to a constant value inside the solid area, as described hereafter, respecting the boundary conditions of the model in use. Secondly, the wall distance y is altered to take into account the presence of the immersed solid. The distance y_{IB} of every cell centre from the IB surface is calculated and then the wall distance is estimated as the minimum between the y_{IB} and the conventional y , in a similar way presented by Mochel et al. [19]. The influence of the wall distance adaptation is visualised by figure 3.

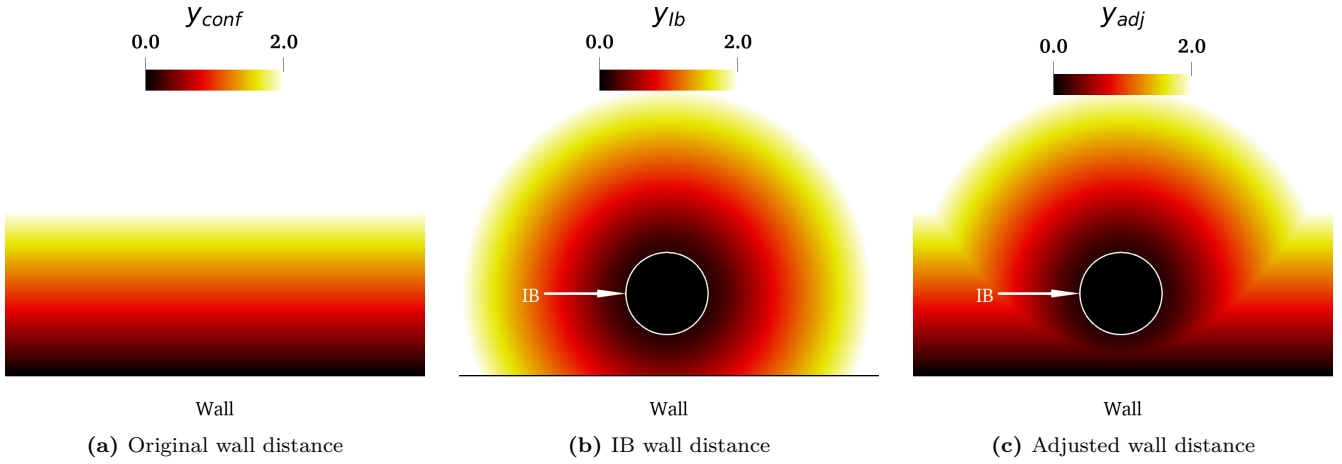


Figure 3: The calculated wall distance for an indicative computational domain with immersed boundaries: the original wall distance considering only conformal walls, seen on the left, is superimposed with the wall distance for the immersed boundary (here a cylinder), seen in the middle, to result in the adjusted wall distance, seen on the right, which takes into account both conformal and immersed walls. In this example, only the lower boundary of the domain is considered as wall boundary. The wall distance is given in units of length.

The Reynolds stresses are modelled using the Boussinesq assumption 2.10. The turbulent viscosity μ_{turb} is estimated by the turbulent model.

$$\tau_R = -\rho \cdot \overline{\mathbf{u}'\mathbf{u}'} = \mu_{turb} \cdot (\nabla \bar{\mathbf{u}} + \nabla \bar{\mathbf{u}}^T) - \frac{2}{3} \rho k \mathbf{I} \quad (2.10)$$

In the present study, for wall bounded flows, the modified low-Re $k - \omega$ SST [48, 60, 61], expressed by the equations 2.11, has been used, incorporating the Reboud correction for multiphase flows [60, 62]. The expressions and the values of the parameters and the empirical constants included in the equations, follow the recommendations by Menter [63], as well as the on-line turbulence modelling resource of NASA [64]. In practice, the constants F_1 , F_2 are functions of, amongst other variables, the inverse of the distance from the wall and thus, the wall distance adaptation was considered essential.

$$\frac{\partial \rho k}{\partial t} + \nabla \cdot (\rho \mathbf{u} k) = \nabla \cdot ((\mu + \sigma_k \mu_{turb}) \nabla k) + \overbrace{P_k - \beta^* \rho k \omega}^{S_k} \quad (2.11a)$$

$$\frac{\partial \rho \omega}{\partial t} + \nabla \cdot (\rho \mathbf{u} \omega) = \nabla \cdot ((\mu + \sigma_\omega \mu_{turb}) \nabla \omega) + \underbrace{\frac{\gamma \omega}{k} P_k - \beta^* \rho \omega^2 + 2(1 - F_1) \sigma_{\omega,2} \frac{\rho}{\omega} \nabla k \nabla \omega}_{S_\omega} \quad (2.11b)$$

$$\nu_{turb} = \frac{\alpha_1 k}{\max(\alpha_1 \omega, \sqrt{2 S_t F_2})} \quad (2.11c)$$

The turbulent model provides an estimate for the turbulent dynamic viscosity ν_{turb} ; then the turbulent viscosity is computed as $\mu_{turb} = f(\rho) \cdot \nu_{turb}$, where the density function $f(\rho)$ is given by 2.12. The effective viscosity, present in the momentum equations 2.1b, is then calculated as $\mu_{eff} = \mu + \mu_{turb}$.

$$f(\rho) = \rho_v + \left(\frac{\rho_v - \rho}{\rho_v - \rho_l} \right)^n \cdot (\rho_l - \rho_v), \quad n = 10 \quad (2.12)$$

To apply the boundary conditions in the area of the immersed boundary, source terms are added in the transport equations of the turbulent variables. In the case of $k - \omega$ SST, the boundary conditions for the turbulent kinetic energy and the specific dissipation are set according to Wilcox [65] to $k_{wall} = 0 m^2 s^{-2}$ and $\omega_{wall} \rightarrow \infty$, practically $\omega_{wall} = 10^{15} s^{-1}$. Therefore, the aforementioned source terms are calculated by 2.13. The turbulent transport equations are solved at the end of the time-step, after the time-advancement of the NS equations.

$$S'_k = \frac{k_{wall} - k}{\Delta t}, \quad S'_\omega = \frac{\omega_{wall} - \omega}{\Delta t} \quad (2.13)$$

Nevertheless, for certain applications adopting another strategy towards turbulence modelling might be necessary. For simple academic laminar simulations the Reynolds stress term is simply disregarded. To adopt a inviscid approach is suffices to set viscosity to zero. On the other hand, Large Eddy Simulations (*LES*) might be preferred for biological or industrial flows with complex and transient dynamics. Coupling the method with LES models seems on first analysis a straightforward task, as the absence of transport equations minimises the required modifications; however, when near wall modelling becomes of high importance the relevant discussions and the solutions of boundary layer reconstruction should be considered [30]. This has not yet been addressed in the current study.

3 Numerical Results

The performance of the presented direct forcing Immersed Boundary method is assessed in well-documented cases and validated against results from the literature or from prior numerical simulations. In the following sections, the method is initially applied on cases of moving cylinders in stationary or flowing incompressible fluid, the incompressible turbulent flow over a backward-facing step and the supersonic compressible flow over a stationary cylinder; then it is evaluated for cavitation inception from a rotating cross in a stationary liquid, as well as the for turbulent cavitating case over stationary and rotating hydrofoils; finally it is applied in the case of cavitation inception at the needle valve closure of a Diesel injector.

3.1 Incompressible Flow over Cylinders

3.1.1 Oscillating Cylinder in fluid at rest

The oscillation of a cylinder in a fluid at rest is simulated, in order to assess the method’s capability to handle moving boundaries. Apart from the Reynolds number, this case is characterised also by the Keulegan-Carpenter number $KC = U_{max}/(f \cdot D)$, where U_{max} refers to the maximum velocity and f the frequency of the oscillation of the cylinder. The motion of the cylinder is described by a harmonic function $x(t) = -A \sin(2\pi ft)$, with $A = KC/2\pi$ the amplitude of the oscillation.

The computations are carried out using air as the surrounding fluid and choosing $Re = 100$, and $KC = 5$, resulting in a Strouhal number $St = 0.2$, to match the experimental data available from Dütsch [66]. The computation run for 8 oscillating periods. Three different meshes are used to determine the mesh influence on the results. In addition, the IB method results are compared to simulations applying an over-set mesh technique, where the cylinder over-set mesh conforms to the solid cylinder boundary.

A $55D_{cyl} \times 35D_{cyl}$ domain is discretised using canonical orthogonal grid; telescopic refinement is used in order to achieve the desired resolution in a square region $[-3D_{cyl}, 3D_{cyl}]$, centered on the equilibrium point of the cylinder’s oscillation. The three meshes yield a cell edge of $5\%D_{cyl}$ (coarse), $2.5\%D_{cyl}$ (medium) and $1.25\%D_{cyl}$ (fine), in the refined region near the cylinder.

In figure 4, the velocity components are plotted for three different phases of the oscillation and on four different cross sections along the oscillation path of the cylinder, for the three meshes, in order to assess the influence of spatial discretisation on the numerical results. The small deviation of the velocity profiles indicate that the immersed boundary method is mesh independent.

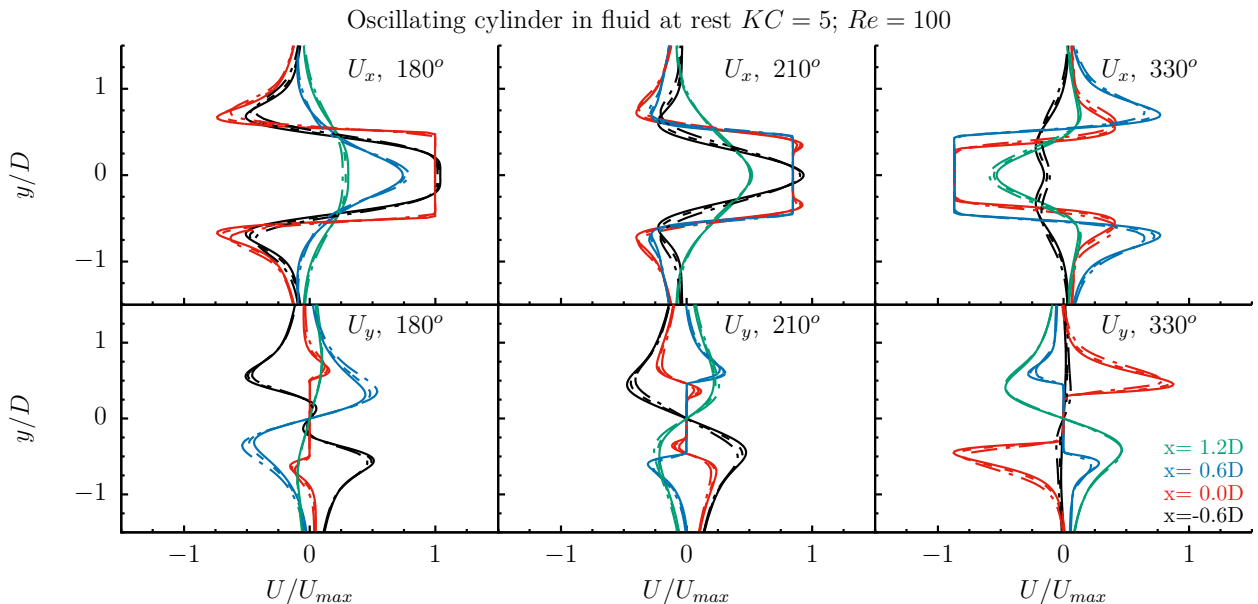


Figure 4: Mesh dependence of in-line (*top*) and cross (*bottom*) velocity for Immersed Boundary simulations of cylinder oscillation in air at rest, at $Re = 100$ and $KC = 5$, at four different cross-sections: coarse (— · —), medium (— — —), fine (continuous line).

In figure 5 the IB method is compared to the experimental data of Dütsch [66], and to an *over-set mesh* methodology, available in OpenFoam+ [67]. According to the over-set mesh approach, two grids are created, one background that does not take into account the moving cylinder and one smaller around the cylinder, which conforms to the geometry; an interpolation procedure is used to communicate field values between the two meshes. The *medium* mesh is used for both numerical simulations. The predicted velocity profiles exhibit a good agreement for the two computational methods, as well as with the experimental data, although some peak values are not captured.

Finally, the drag coefficient over the length of the cylinder, computed as $C_D = 2f_x/(\rho D_{cyl} U^2)$, is plotted for the IB method, the over-set mesh and the experiments, in figure 6, where IB simulations for the three different meshes are compared in plot 6a for $dt = 0.5ms$ and for three different time steps using the medium mesh in plot 6b. Both methods

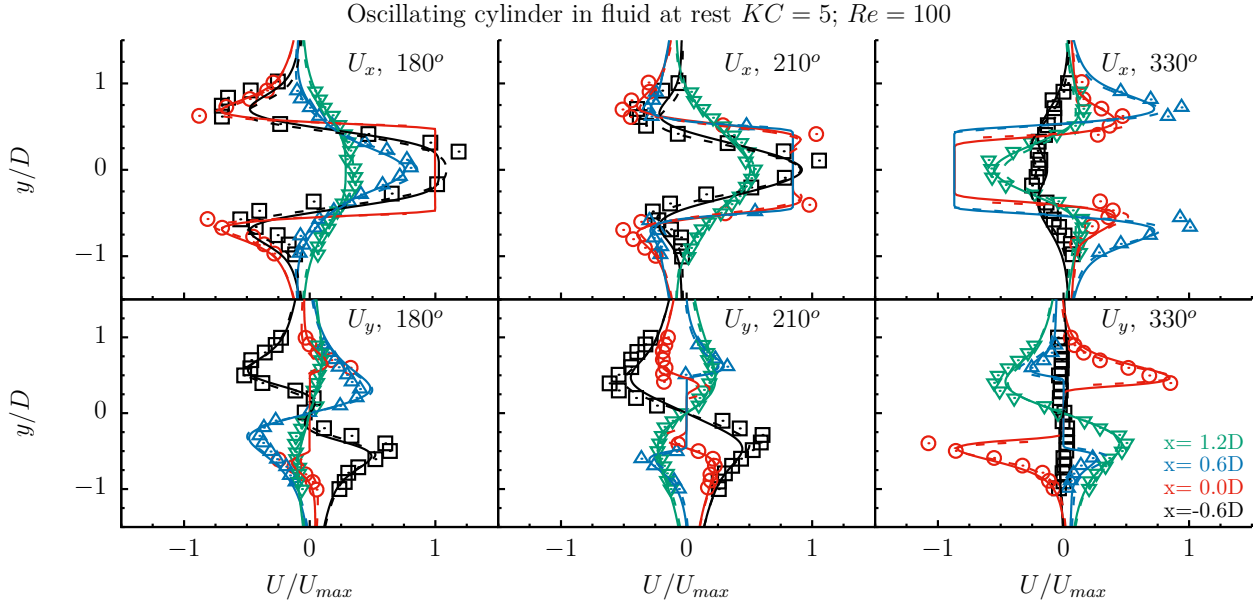


Figure 5: Comparison of in-line (*top*) and cross (*bottom*) velocity profiles for Immersed Boundary simulations (*continuous line*) of cylinder oscillation in air at rest, $Re = 100$ and $KC = 5$, to over-set mesh computations (*dashed line*) and Dütsch et al. [66] experimental data (*symbols*), at four different cross-sections.

produce results that coincide with experimental data. However, it can be observed that the over-set curve has a lot of spikes, whereas the IB curves are smoother. If the over-set method was to be used in the framework of a flow-induced motion for the cylinder, these spikes might result in non-convergent simulation and highly unsteady motion. In contrast, the IB method seems more suitable for such complicated fluid-structure interaction problems.

For the IB curve, the smoothness is influenced by the spacial and temporal resolution. A coarser grid yields weak force spikes in some parts of the oscillation, probably because the immersed body representation is not accurate enough. On the other hand, a larger time-step provides a smoother curve. The time step and minimum cell size control the percentage of a masked (solid) cell to be revealed and of an unmasked (fluid) cell to be covered by the immersed body as it moves and therefore affects the unsteadiness of the forcing source term.

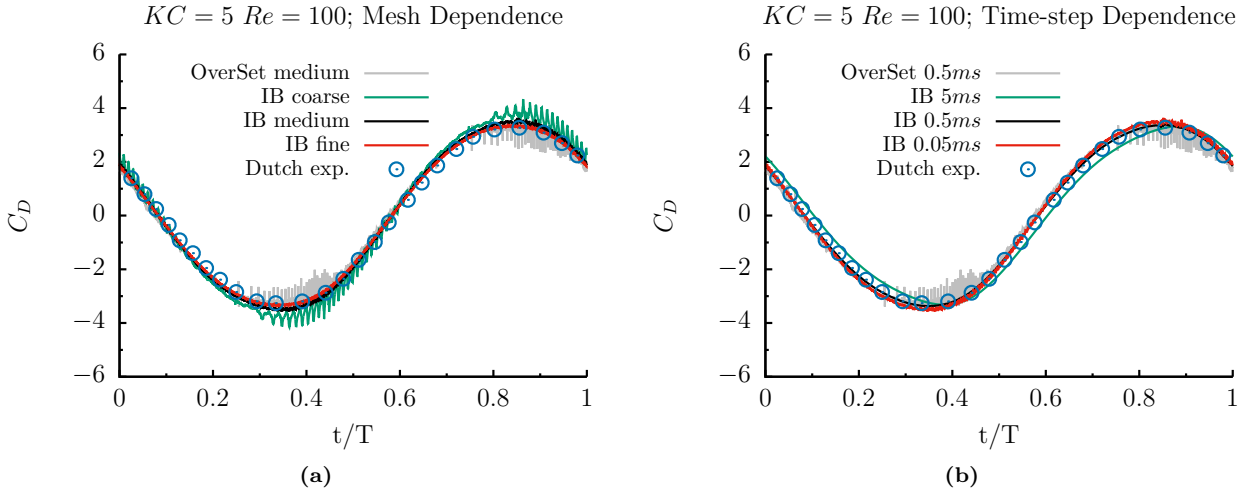


Figure 6: Comparison of drag coefficient for Immersed Boundary simulations with the three different meshes (*left*) and three different time steps (*right*), to the computation of the over-set mesh technique (using the fine mesh) and the experimental data of Dütsch et al. [66].

3.1.2 Flow past oscillating Cylinder

The next benchmark case considered to assess the performance of the proposed Immersed Boundary method is the case of an incompressible flow development over an in-line oscillating cylinder. The current Finite Volume IB method simulation results are compared with the numerical data of Hurlbut et al. [68], obtained using the Finite Difference approach.

The computations of Hurlbut et al. [68] were performed on a fixed grid, conforming to the cylinder surface. The oscillating motion of the cylinder was taken into account using a non-inertial coordinate transformation, where the

velocity of the fluid is divided in to two components: one relative to the moving cylinder (\mathbf{U}_f) and one relative to the inertial frame of reference (\mathbf{U}_r). The latter is calculated as a function of time, representing the oscillation of the cylinder.

The cylinder is initially stationary, exposed in a flow of $Re = 100$, until a periodic vortex shedding is achieved. Then, it starts to oscillate at a frequency twice as the Strouhal number of the vortex shedding, which is calculated as $St_q = f_q U_{inf} / D_{cyl} = 0.166$, where f_q the vortex shedding frequency; this is in agreement with the literature [69–71]. According to Hurlbut et al. [68], at such an oscillation frequency, phase locking is observed which increases the drag and maximizes the lift coefficient.

As in the previous case, air is chosen as the medium and the velocity of the cylinder is described by the equation $u_c(t) = 2\pi f_c A \cos(2\pi f t)$, with the amplitude of the oscillation subject to the constrain of $KC = 5$ and $f_c = 2f_q$, where f_c the oscillation frequency of the cylinder.

The computational domain is chosen to be $L = 55D_{cyl}$ in length and $H = 35D_{cyl}$ in height, and discretised by an orthogonal Cartesian grid, which makes use of telescopic refinement near the cylinder and along the vortex street, to yield square cells with edge length of $\delta x = \delta y = 1\%D_{cyl}$.

Comparison of the drag (C_D) and lift (C_L) coefficient, extracted from the IB simulations, against the conformal grid computational data of Hurlbut et al. [68], show excellent agreement, as illustrated in figure 7. The current IB method provides accurate results and greatly simplifies the computational procedure compared to the numerical setup of Hurlbut et al. [68]

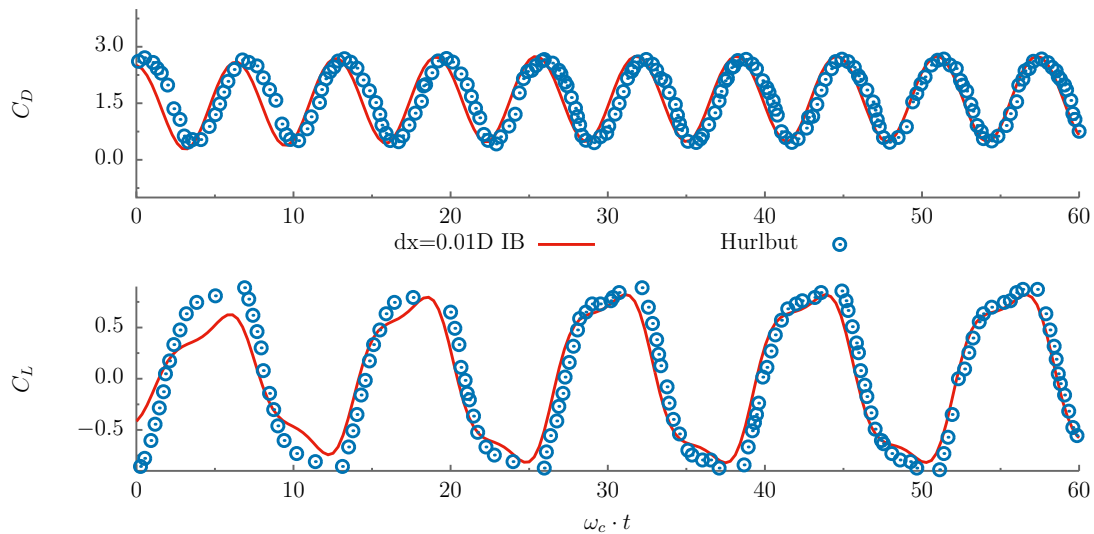


Figure 7: Flow over oscillating cylinder at $Re = 100$. Comparison of Lift (*top*) and Drag (*bottom*) coefficient for Immersed Boundary simulations (*lines*) to conformal grid computational data of Hurlbut et al. [68] (*symbols*). The cylinder oscillates at a frequency two times greater than the vortex shedding frequency, $f_c = 2 \cdot f_q = St_q \cdot U_{inf} / D_c$.

3.2 Turbulent flow over backfacing step

In order to test and validate the treatment of turbulent modelling by the presented Immersed Boundary method, a widely accepted benchmark case of the flow over a back-facing step [72–75], at a Reynolds number of $Re = 69610$, is studied. The present numerical simulation results are compared to the experimental data provided by Kim [72].

The case consists of the incompressible flow of air ($\rho = 1.88553 \text{ kg/m}^3$, $\mu = 1.83698 \cdot 10^{-5} \text{ kg/ms}$) in a channel, over a back-facing step. The total height of the channel is $H_{Total} = 3h$, where h the height of the step. The step extends $L_1 = 4h$ downstream the inlet. The outlet is placed $L_2 = 61.4h$ downstream the step. The domain, which can be seen in figure 8a, matches the configuration reported by [73], who simulated the same flow using curvilinear grids. The step is represented as an Immersed Boundary, as seen in figure 8b.

Unsteady Reynolds-Averaged (URANS) computations are carried out and the $k - \omega SST$ turbulent model is used. In addition to IB simulations, conformal grid simulations are also performed. Thus the performance of the IB method is evaluated, with respect to the accuracy of solver.

The conformal grid yielded $y^+ = 40$ near the wall. For the IB simulations, two different grids were used; a coarse achieving $y^+ = 40$, similar to the conformal grid, and a fine reaching $y^+ = 10$. When using an Immersed Boundary, is not trivial to determine the height of the first cell over the (immersed) wall, as the grid generally does not conform to the solid wall and the normal to the boundary direction does not coincide with the cell height. Therefore the y^+ serves rather as an indication of the grid resolution than an absolute characteristic measure of the turbulent modelling. In this particular case however, the computational cells are aligned with the immersed wall, therefore the y^+ retains its physical significance.

In figures 9 and 10, the profiles of turbulence kinetic energy (TKE) and in-line velocity (U_x) respectively, along different vertical sections downstream of the step, are plotted. The numerical results of the IB method are compared to the conformal grid results and the experimental data of Kim [72]. Good agreement is found between the two numerical methods and the deviation of both from the experimental results is small. Moreover, the Immersed Boundary

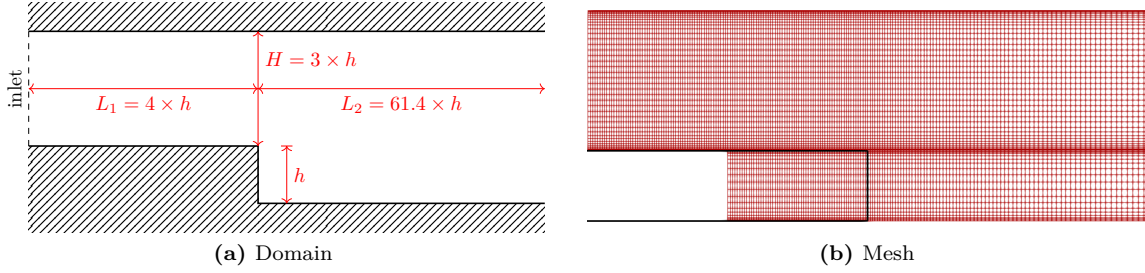


Figure 8: Computational domain (*left*) and mesh with IB surface (*right*) for back-facing step case. Geometric expansion of the cell height is used to refine the canonical orthogonal mesh near the wall and the top side of the step and achieve the desired y^+ value.

computations' results prove independent of the grid resolution over the step. However, both numerical methods do not capture accurately the velocity profile in the recirculation region (first four sections in figure 10), as well as they both underestimate the maxima of the curves. In addition, small differences are observed in the distributions of turbulent kinetic energy between the IB method and the conformal grid simulation, as the IB method overestimates turbulence near to the step (first two sections in figure 9).

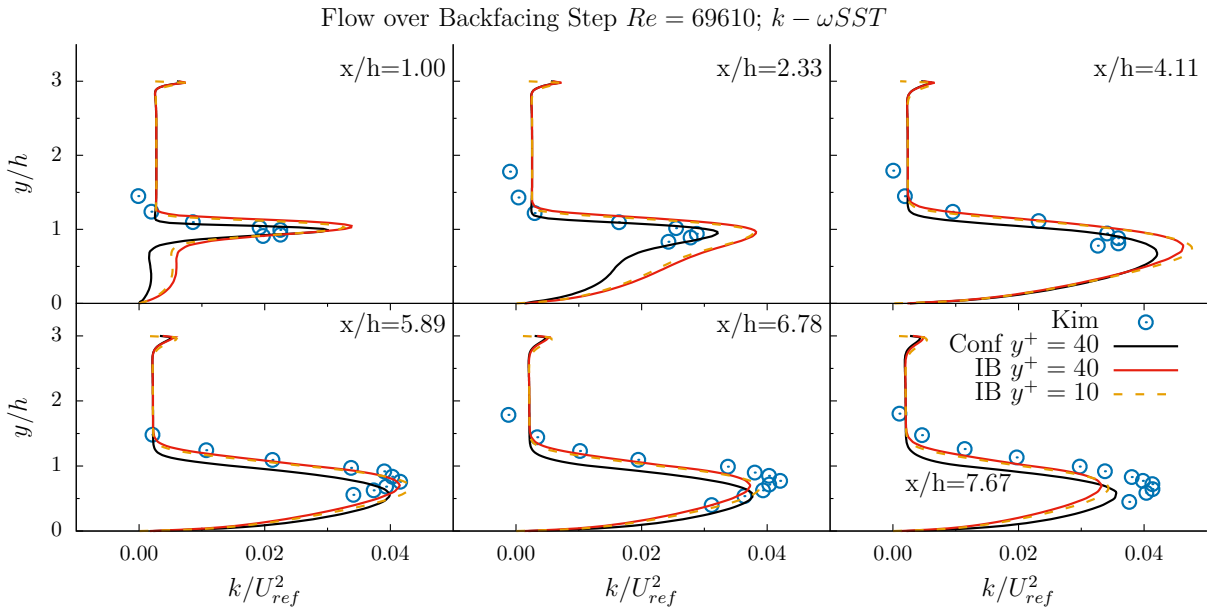


Figure 9: Flow over back-facing step. Turbulent Kinetic Energy vertical distribution on six different positions along the channel. Immersed Boundary results for coarse (*red line*) and fine mesh (*dashed orange line*) compared to conformal grid computations (*black line*) and experimental data of Kim et al. [72] (*symbols*).

3.3 Supersonic Flow past Cylinder

In order to assess the performance of the IB methodology coupled with the density-based solver, a well-known benchmark case of supersonic flow past a cylinder is examined. Such a flow is well known for the bow-shock formation upstream of the rigid body and empirical relations exist for its stand-off distance.

According to the work of Billing [76], the exact hyperbolic shape of the detached shock can be derived, based on the radius R of the cylinder, the body stand-off distance Δ_s and the vertex radius of curvature R_c of the shock. The latter two parameters depend on the dimensionality of the problem and the Mach number of the flow; for a cylinder in 2D they are given by relations 3.1. These relations are correspond to low temperature experiments and perfect gas assumption, while for real gases these values are reduced.

$$\Delta_s/R = 0.386e^{4.67/Ma^2} \quad \text{and} \quad R_c/R = 1.386e^{1.8/(Ma-1)^{0.75}} \quad (3.1)$$

Herein, the $Ma = 2$ and $Re = 300$ flow over a cylinder is considered. Gas is chosen as the working fluid, with the properties of air at 300K: $\mu = 1.846 \cdot 10^{-5} kg/ms$, $c_s = 347.336 m/s$ and $\rho_{init} = 1.177 kg/s$. Temperature effects are neglected for this assessment study.

The computational domain is chosen to be $55D_{cyl} \times 35D_{cyl}$, discretised using a Cartesian homogeneous grid and telescopic refinement is employed to increase the spatial resolution in the vicinity of the cylinder. Three different grids are considered yielding a minimum cell edge of $dx = 7.4\%D_{cyl}$ (coarse), $dx = 3.7\%D_{cyl}$ (medium) and $dx = 1.9\%D_{cyl}$

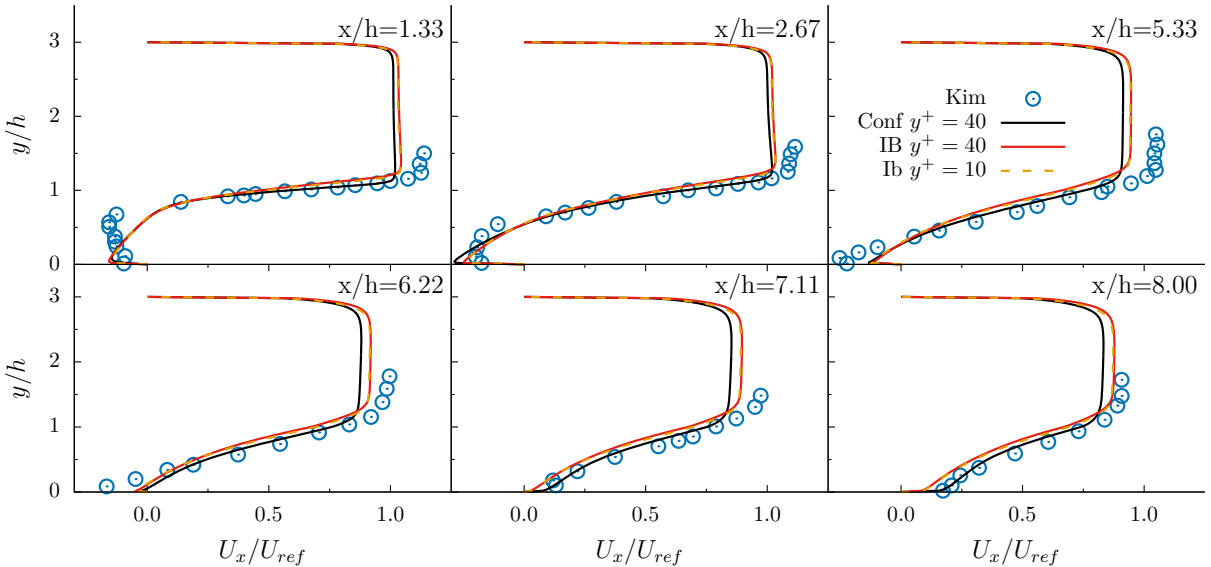


Figure 10: Flow over back-facing step. In-line velocity profile on six different positions along the channel. Immersed Boundary results for coarse (red line) and fine mesh (dashed orange line) compared to conformal grid computations (black line) and experimental data of Kim et al. [72] (symbols).

(fine) in the area of the cylinder. In addition, two conformal mesh computations are carried out; one on a *C-type* grid, with a resolution of approximately $dx = 6.3\%D_{cyl}$ on the cylinder’s wall, and one a *Cartesian-cut* grid derived from the coarse IB grid with one level of refinement on the cylinder’s wall. The different mesh approaches are illustrated in figure 11.

The model 3.1 predicts $\Delta_s = 1.24R = 0.62D_{cyl}$. From the three IB simulations we get $0.66D_{cyl}$ for the coarse, $0.47D_{cyl}$ for the medium and $0.45D_{cyl}$ for the fine mesh, while for the conformal grid simulations we get $0.65D_{cyl}$ for the Cartesian-cut and $0.52D_{cyl}$ for the C-grid. In addition the drag coefficient C_D for the IB simulations are estimated as 1.36 for the coarse, 1.45 for the medium and 1.5 for the fine mesh. For the conformal grid simulation the Cartesian-cut mesh predicts 1.37 and the C-grid 1.5. For the same problem using different Immersed Boundary techniques, Riahi et al. [20] predict $\Delta_s = 0.69D_{cyl}$ and $C_D = 1.51$ and Takahashi et al. [25] report $C_D = 1.4 - 1.6$. The predicted stand-off distance can be further compared with values found the literature [77] in figure 14a.

It can be seen that the proposed methodology tends to under-predict the stand-off distance of the shock, while it gives an accurate estimate of the drag coefficient. The influence of the spatial resolution on the results, which is also apparent for the conformal grids, seems inevitable for the explicit density-based algorithm employed, which might be sensible in the spatial interpolation schemes; further investigation of this matter exceeds the scope of the current paper.

In addition, the consistence between the results on the Cartesian-cut and the coarse IB grids, which are of the same spatial resolution in the entire domain, provides proof of the accuracy of the proposed IB method. This is also supported by good agreement of the velocity profiles shown in figure 12 and the density contours that visualise the bow-shock in figure 13. Finally, in figure 14b the pressure recuperation downstream of the cylinder is shown, where the influence of the density of the grid is evident; the results on the Cartesian-cut conformal grid is closer to the IB results.

3.4 Cavitation Induction by Rotating Cross

Following the benchmark incompressible cases, with moving or stationary immersed bodies, laminar or turbulent regimes, the present Immersed Boundary method is applied onto cavitating flows. The case of cavitation induced by a rotating cross immersed into stationary water, which could be seen as a case of an idealised propeller, is presenter hereafter.

The instantaneously started rotation of the cross from idle, accelerates the surrounding stationary liquid and induces cavitation. This test case was studied by Örley et al. [35] to validate their cut cell immersed boundary method against a simulation using a Arbitrary Lagrangian-Eulerian formulation (*ALE*)(with conformal to the geometry grid). In the present study, an additional simulation with a conformal to the cross geometry grid, employing a sliding mesh approach using Arbitrary Mesh Interface (*AMI*) [78] method, is carried out in order to compare with the developed Immersed Boundary method.

The cross consists of a circular hub with diameter $d_{hub} = 0.2 m$ and two bars of the same thickness $w_{bar} = 0.1 m$ but different length, $l_1 = 1.0m$ and $l_2 = 0.5 m$. As computational domain is chosen a square with edge length $L_{sq} = 600l_1$ and is discretised by a canonical Cartesian grid. Three different mesh resolutions are used, as in the referenced work [35], one with 10 cells (coarse mesh) along the thickness of the bars w_{bar} , one with 20 cells (medium mesh) and one with 40 cells (fine mesh). Several levels of telescopic refinement are used to achieve the desired resolution in an area $2l_1 \times 2l_1$ around the center of the hub of the cross.

The initial ambient pressure is set to $p_{init} = 1 bar$, the liquid is initially at rest and the angular velocity of the cross

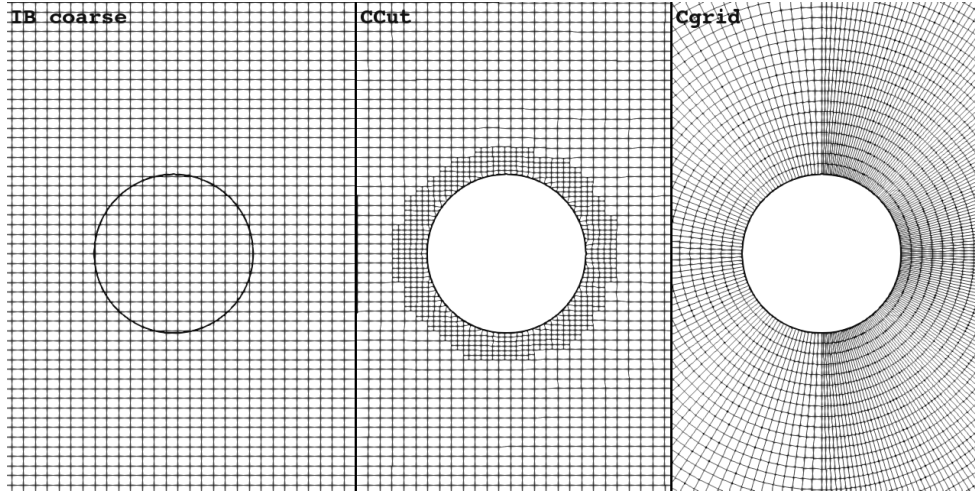


Figure 11: Computational domain and meshes used in Immersed Boundary and conformal grid simulations of super-sonic flow past cylinder at $Ma = 2$ and $Re = 300$. These grids refer to the coarse (IB $7.4\%D_{cyl}$) IB mesh, Cartesian-cut (CC $7.4\%D_{cyl}$) and C-grid (CG $6.3\%D_{cyl}$) conformal meshes.

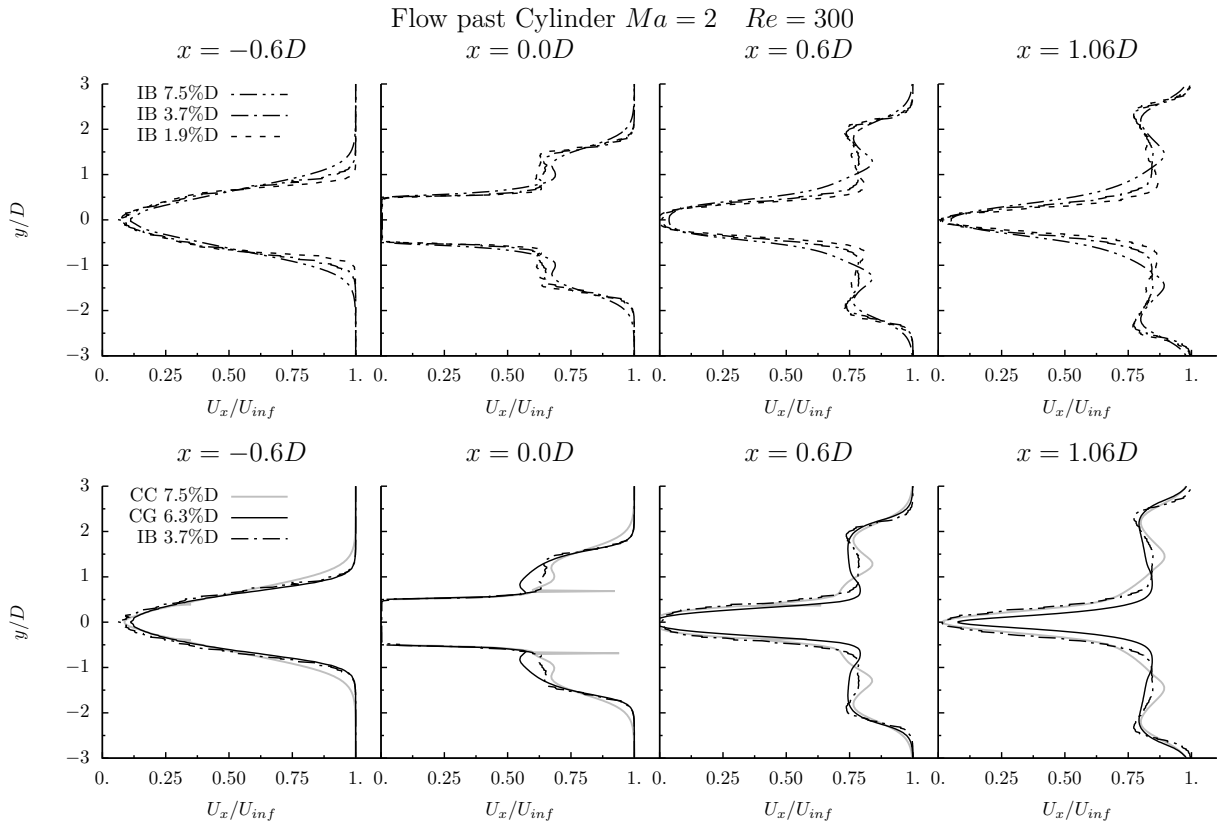


Figure 12: Mesh dependence of in-line velocity profiles for Immersed Boundary simulations of super-sonic flow past cylinder at $Ma = 2$ and $Re = 300$, at different cross sections along axis of symmetry. Three different grids are considered: coarse (IB $7.5\%D_{cyl}$), medium (IB $3.7\%D_{cyl}$) and fine (IB $1.9\%D_{cyl}$). Results are compared with conformal grid simulation (CG $6.3\%D_{cyl}$ and CC $7.4\%D_{cyl}$).

is $\omega = 20 \text{ rad/s}$ around the axis perpendicular to the plane. The density of the liquid water is $\rho_L = 998.16 \text{ kg/m}^3$ and for the saturated vapour $\rho_V = 0.017312 \text{ kg/m}^3$, while the saturation pressure is set $p_{SAT} = 2339 \text{ Pa}$. The Wallis formula is used for the mixture's compressibility calculation.

As the cross starts to move, the ambient liquid is abruptly accelerated, pressure drops along the cross surface, small vapour structures are formed and strong pressure waves are emitted radially away from the solid boundary, visible in figure 15. These waves get superimposed while traveling away resulting in a complex pressure field. These initial vapour structures will then collapse and as the velocity field is developed, cavitation will be induced on the path of the cross, on the top of the long bars and near the convex surface of the hub. As these vapour structures collapse, new strong pressure waves are emitted towards the far field, as it can be seen in the sequence plots of figure 16.

Comparison of the vorticity contours for the different meshes and the AMI simulation, presented in figure 17, show that mesh resolution affects greatly the sharpness of the contours, with different structures visible on the finer mesh, which leads also to different vapour structures. In addition, the conformal mesh simulation (AMI approach) exhibit

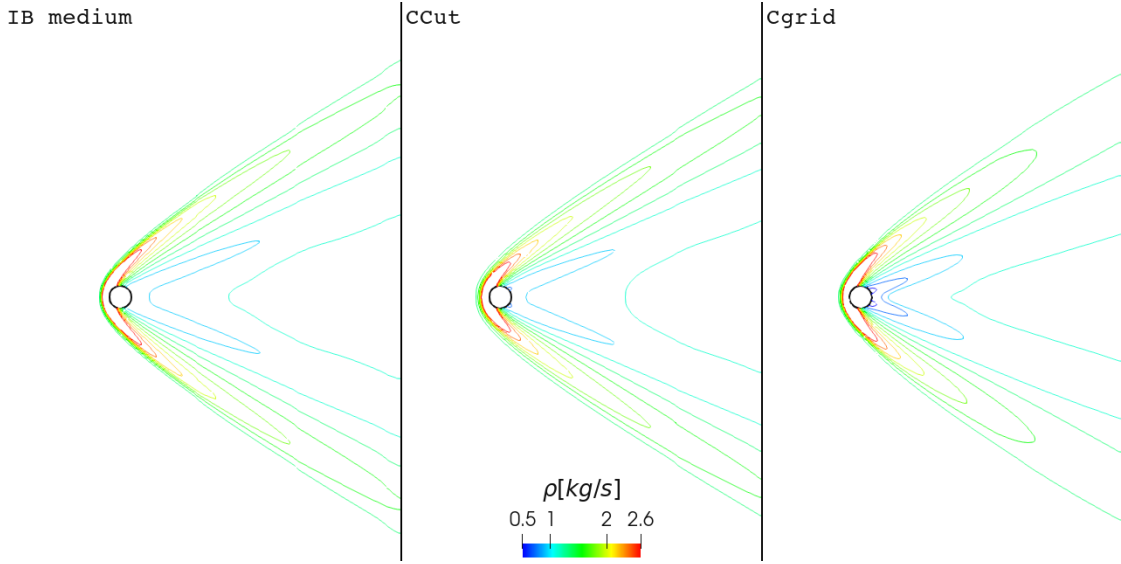


Figure 13: Density contours and bow-shock visualisation for Immersed Boundary and conformal grid simulations of super-sonic flow past cylinder at $Ma = 2$ and $Re = 300$.

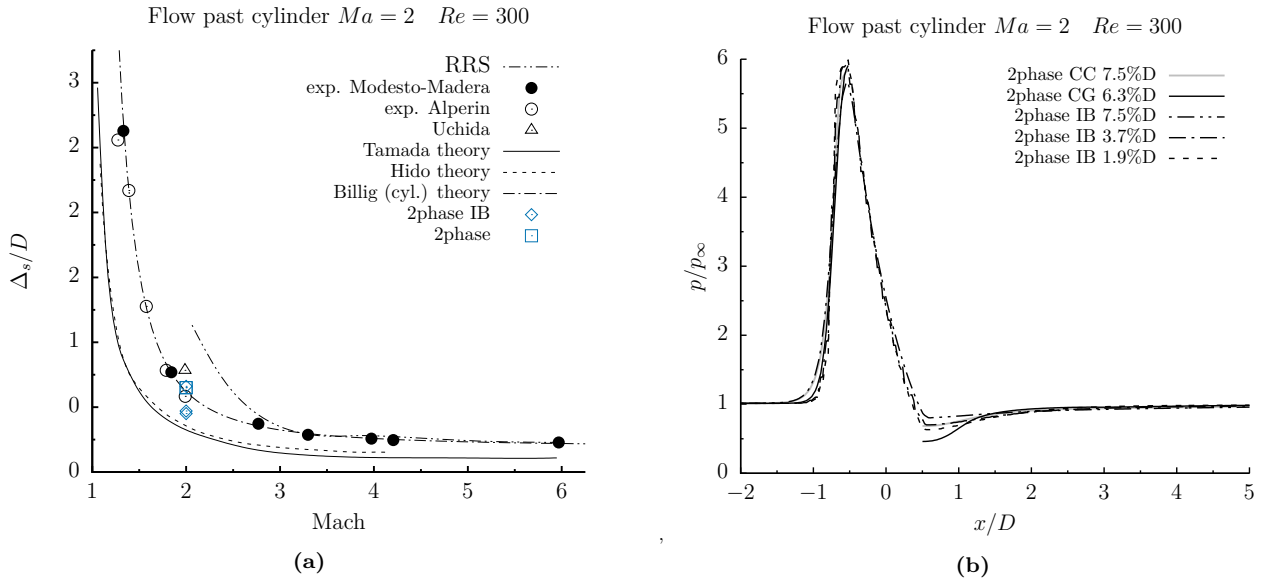


Figure 14: Shock stand-off distance (a) and pressure along symmetry axis (b), for simulations using Immersed Boundary (*2phase IB*) and conformal grid (*2phase*), wither with cartesian-cut (*CC*) or C-type grid (*CG*), of super-sonic flow past cylinder at $Ma = 2$ and $Re = 300$. Data for the stand-off extracted from literature [76, 77].

different vorticity and vapour structures than the IB computations, and capture weak vapour formation near the convex surface of the hub.

The total amount of vapour created during one full rotation of the cross is plotted in figure 18, for the different grids, the AMI approach as well as the cut cell (both *10 cells* and *20 cells* meshes) and the ALE simulations reported by Órley et al. [35]. It can be seen that the current IB method, for the medium grid, although it results in a curve that follows closely the respective medium grid computation with cut cells [35] but reaches a larger maximum, predicts greater vapour creation, than all the other computations. Finer grid resolution enhances the vapour creation, as expected. In addition, it can be observed that the conformal grid simulations give different predictions, which might be linked to the different solvers or barotropic models used.

The velocity magnitude contours, plotted in figure 19 for three phases of the oscillation, for the computation with the medium grid, differ slightly from the AMI simulation, whereas the vapour structures show greater deviation. The difference becomes more apparent for the 360° degrees, where the velocity contours, the vapour distribution, and therefore the velocity streamlines, show significant differences.

Although differences can be noted between the IB and the AMI simulations, the current immersed boundary method proves adequate and suitable for treating cavitating flows with moving boundaries. The physics is captured, including pressure waves and vapour creation, growth and collapse.

Moreover, the assessment of the performance of the IB in comparison with the AMI approach, has to take into account the computational cost of the simulations. While the IB computation requires a uniform grid on a rather wide area to cover the path of the rotating cross, and results in a grid with approximately 3 times more cells than the one used in

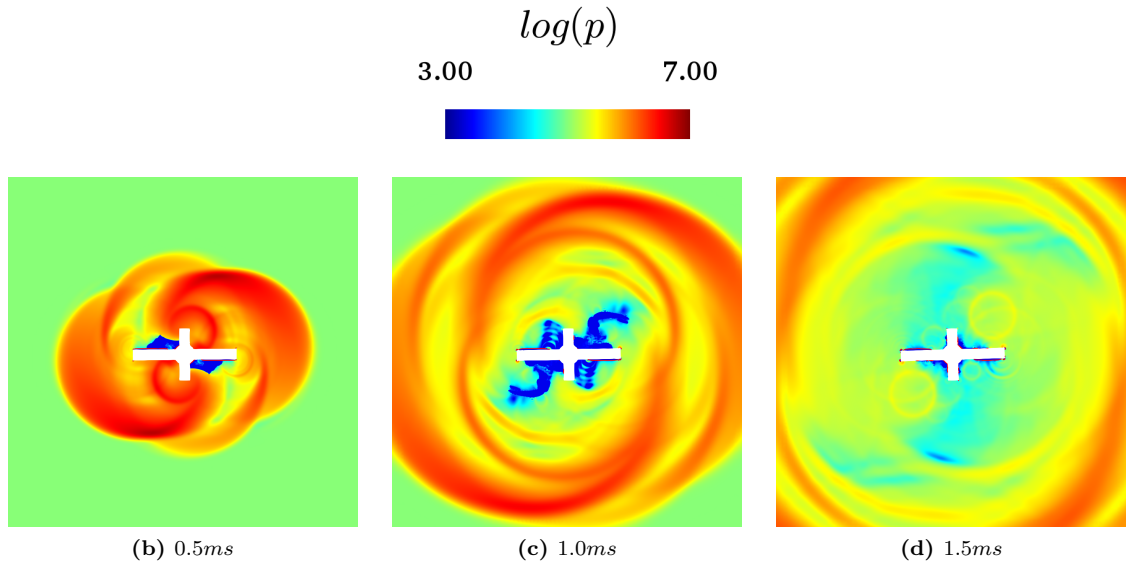


Figure 15: Pressure contours in logarithmic scale (*common logarithm* $\log_{10}(\cdot)$), at the initial stages of the rotation of the cross inside initially stationary water. The time instances are extracted for the fine (40 cells) mesh. One complete rotation lasts 314 ms. Vapour volume fraction of 1% iso-line is plotted with red.

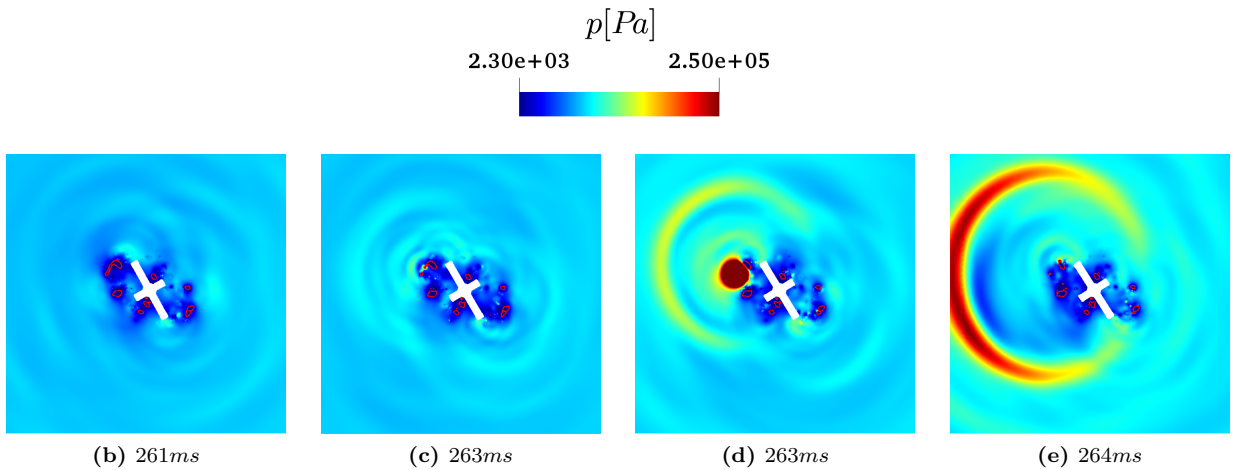


Figure 16: Pressure contours in logarithmic scale (*common logarithm* $\log_{10}(\cdot)$), at the later stages of the rotation of the cross inside initially stationary water. The time instances are extracted for the medium (20 cells) mesh. One complete rotation lasts 314 ms. Vapour volume fraction of 1% iso-line is plotted with red.

the AMI computation, it requires 5 times fewer computational resources. More precisely, the medium grid employed, composed of 185k cells, required 83 cpuh to complete, while the conforming sliding grids of 76k cells, used with AMI technique, required 400 cpuh. The advantages of the IB methodology are apparent.

Finally, in figure 20 a comparison between the solvers coupled with the IB is performed. The explicit density-based algorithm captures a sharper pressure field than the implicit pressure-correction algorithm, as it is observed by comparing figures 20e and 20f with 20b and 20c respectively. The density-based algorithm also predicts larger vapour cavities, as show in the latter figures, which is also reflected in the integral vapour volume fraction of plot 21a. These differences are partially due to the native differences between density and pressure based solvers, the iterative algorithm of the pressure-based solver that might smooth out small variations captured by the density solver, as well as to the coupling with the IB forcing source term. The effect of the treatment of the forcing source term becomes apparent also in the plot of 21a, where the differences of linearised, via equation 2.9, and non-linearised forcing term, coupled with the pressure-based solver, are visualised. On the other hand, figure 21b shows effect of different cavitation models, namely the Wallis and the linear, on the prediction of vapour volume production, with the latter giving slightly higher peak value.

3.5 Cavitating Flow over a Stationary Hydrofoil in channel

Another well-known benchmark case of cavitating flow is the flow over the circular leading edge (*CLE*) symmetric hydrofoil, studied experimentally and numerically by Dular et al. [79]. The complexity of the unsteady cavitating flow poses an important challenge to the presented modelling approach and the available experimental data offer an excellent opportunity to validate the performance of the method.

In the experiment [79], a symmetric hydrofoil, 107.9 mm long and 16 mm thick, is placed in a 50 mm long and 100 mm high cavitation tunnel, at a 5° incidence angle. Both the hydrofoil and the tunnel are 50 mm wide, but the simulations

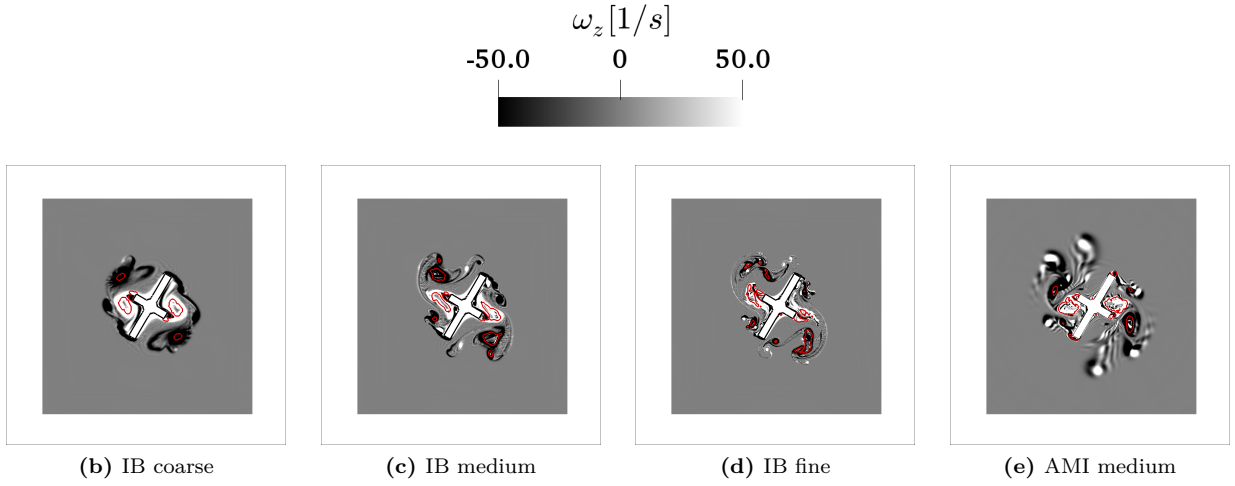


Figure 17: Vorticity contours for rotating cross in water at rest, at 240° . Current *direct forcing* Immersed Boundary method simulations for coarse (a), medium (b) and fine mesh (c) are compared to sliding mesh computations (d) using AMI technique. Vapour volume fraction of 1% iso-line is plotted with red.

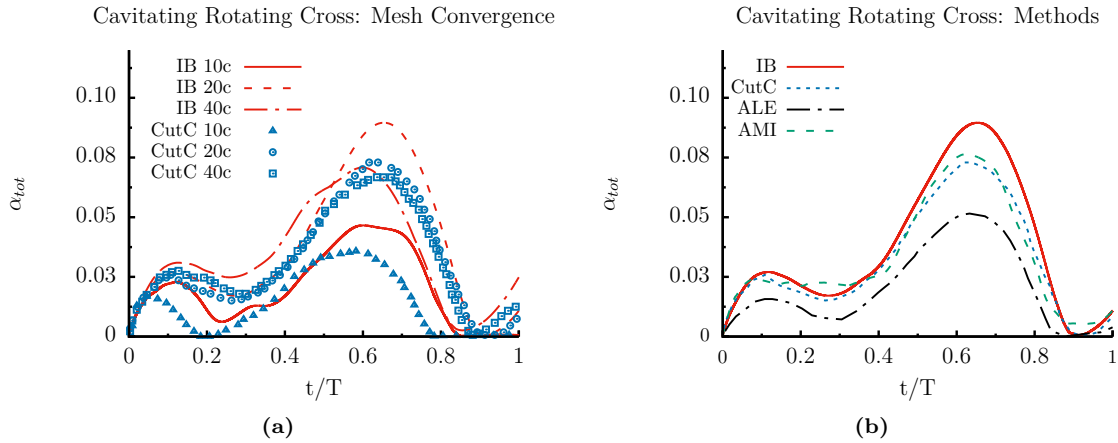


Figure 18: Integral vapor volume fraction's time evolution for rotating cross in water at rest. Mesh convergence comparison between current direct forcing IB method (*IB*) and cut-cell method (*CutC*) from Örley et al. [35], on the left. In addition, a comparison of different computational approaches is presented on the right, between the current IB method, using the pressure-based (*pres. IB*) and the density-based (*dens. IB*) solvers, and the cut-cell calculations, conformal sliding mesh simulations performed using *AMI* approach and *ALE* results reported in the work of Örley et al. [35].

presented hereafter are two-dimensional for simplicity, as the numerical study accompanying the experiments [79]. The computational domain and grid used in the current study can be seen in figure 22. A constant velocity U_{in} is imposed as boundary condition at the inlet on the left side of the domain and a constant pressure p_{out} is set as an outlet boundary condition on the right side. The value of pressure on the outlet is derived from the desired cavitation number of the flow $\sigma = (p_\infty - p_{vap})/(\rho U_\infty^2/2)$. On the upper and lower side are considered no-slip walls.

The computational domain is discretised by a hexahedral orthogonal grid with additional refinement on the interface of the hydrofoil. On the side walls, the cell height reaches values of $y^+ = 30$, whereas near the hydrofoil the cell size is equivalent of $y^+ = 20$. The final grid is composed by 100k hexahedral cells.

The density and kinematic viscosity for water are set to $\rho_l = 998.16 \text{ kg/m}^3$ and $\nu_l = 10^{-6} \text{ m}^2/\text{s}$, and for the saturated vapour $\rho_v = 0.017312 \text{ kg/m}^3$ and $\nu_v = 5.12 \cdot 10^{-4} \text{ m}^2/\text{s}$. The saturation pressure is $p_{SAT} = 2339 \text{ Pa}$.

From the test-cases presented by Dular et al. [79], the current study focuses on *Test 1*, with $U_{in} = 13 \text{ m/s}$ and $\sigma = 2$, for which experimental time-averaged velocity measurements are reported on different sections over the suction side of the hydrofoil, seen in figure 23. The resulting Reynolds number of the flow is $Re = 1.4 \cdot 10^6$.

In the current study, a modified $k - \omega$ *SST* turbulent model, employing the *Reboud correction* for the turbulent viscosity, is used. The simulations is run for few shedding cycles, with the time-step being limited by the *acoustic Courant Number* to be under 2. This yields time-steps of the order of 10^{-6} s . The velocity is sampled on the same sections as the experiments every $0.5 \cdot 10^{-4} \text{ s}$, and then time-averaged to produce velocity profiles to be compared with the referenced experimental data [79]. The comparison of the velocity profiles is presented in figure 24, for the in-line (24a) and cross direction (24b) components.

The comparison yields almost perfect match between the numerical and experimental profiles for the U_x velocity component, while for the U_y component a slight deviation is observed that weakens towards the upper wall. The measured U_y velocity at section $y = 0 \text{ mm}$ receives strictly negative values after $x = 50 \text{ mm}$ while the current computation predicts

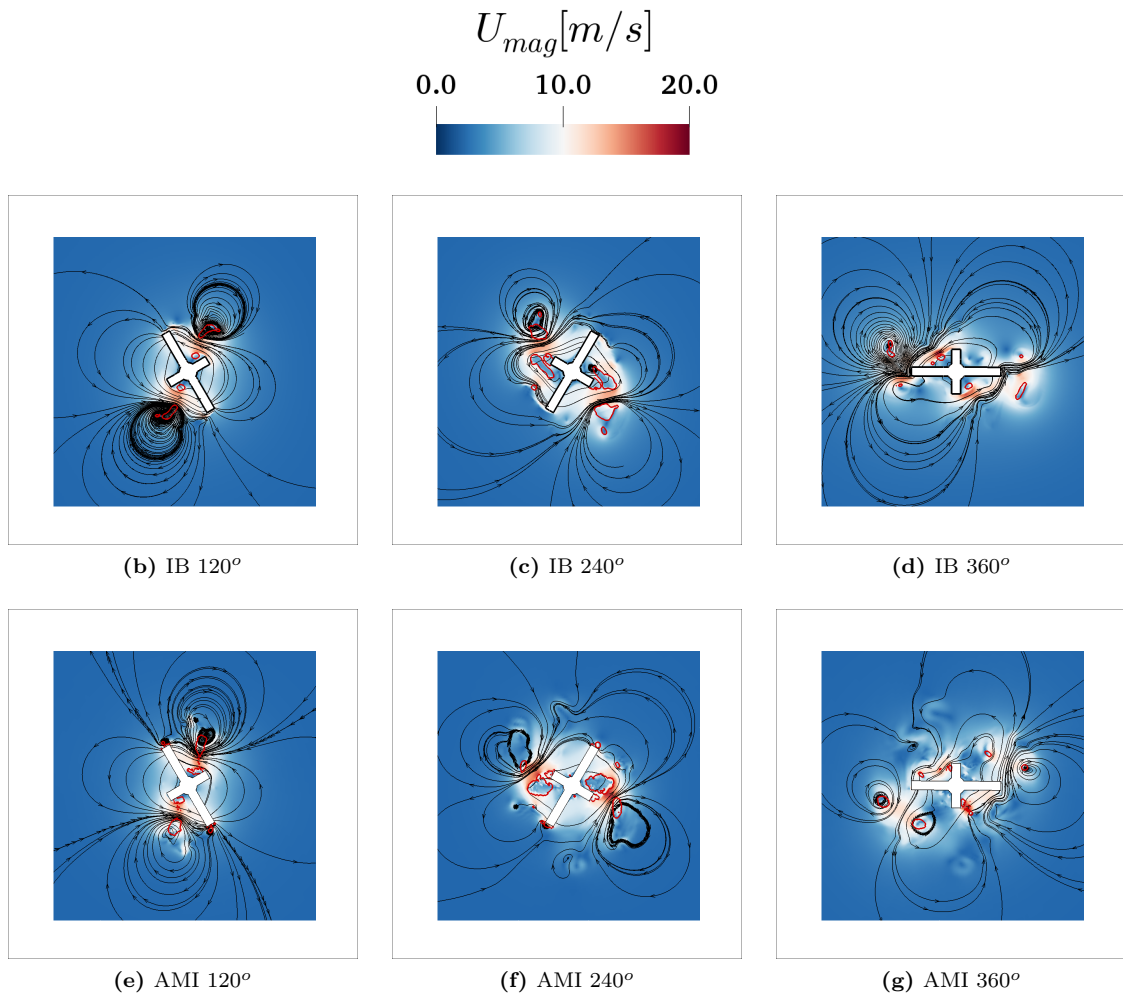


Figure 19: Velocity magnitude contours along with streamlines for IB (*top*) and AMI (*bottom*) simulations for rotating cross in water at rest, at three different rotation angles, for the medium mesh (*20 cells along w_{bar}*). Vapour volume fraction of 1% iso-line is plotted with red.

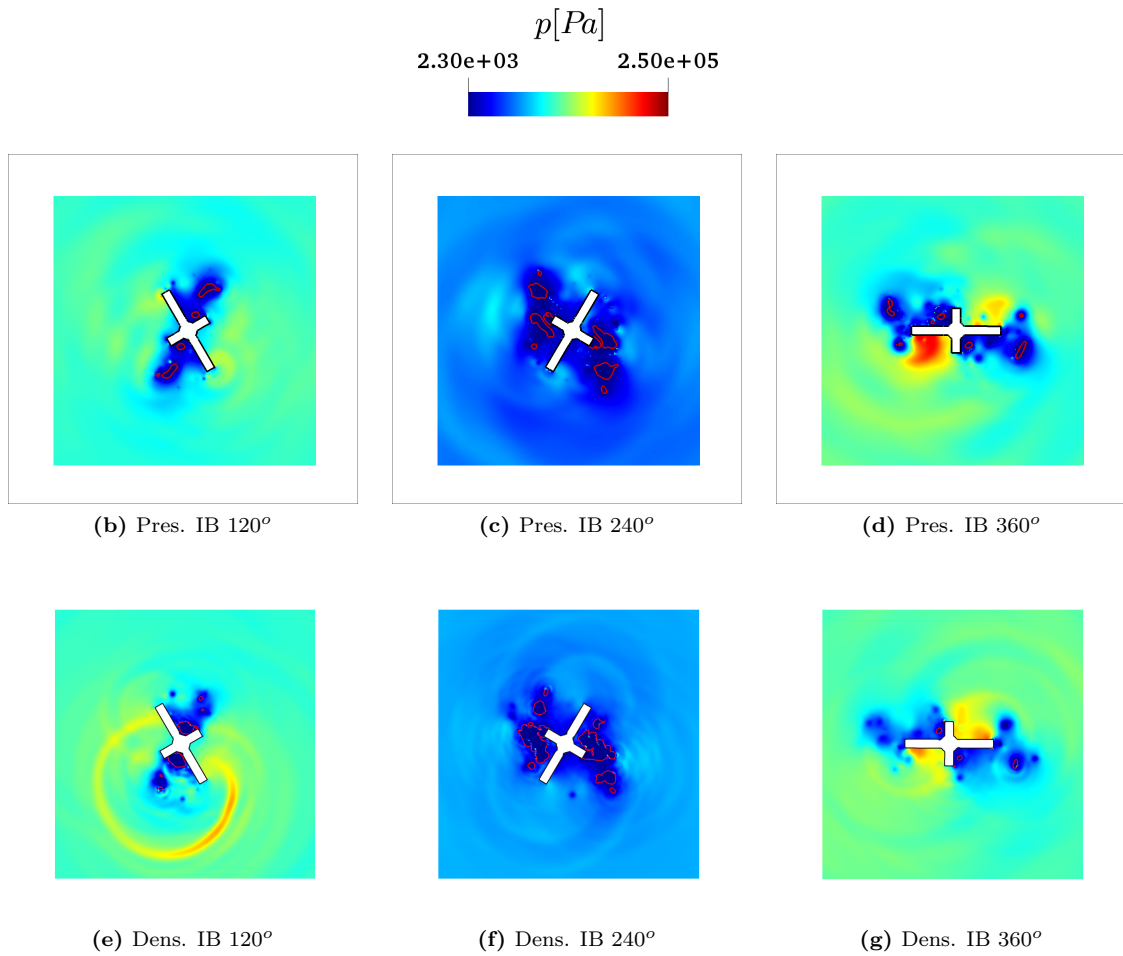


Figure 20: Pressure contours for pressure-based (*top*) and density-based (*bottom*) IB simulations for rotating cross in water at rest, at three different rotation angles, for the medium mesh (*20 cells along w_{bar}*). Vapour volume fraction of 1% iso-line is plotted with red.

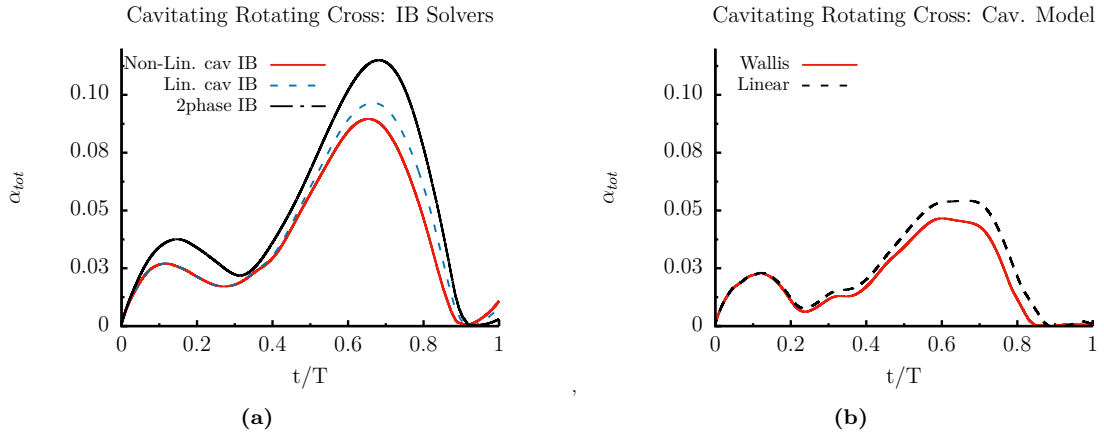


Figure 21: Integral vapor volume fraction's time evolution for rotating cross in water at rest. Sensitivity of IB simulations on computational algorithm on the left and on the cavitation model on the right. Curves on the left refer to the medium mesh (20 cells along w_{bar}) and correspond to the pressure-based solver, with linearised (*Lin. cav IB*) and non-linearised (*Non-Lin. cav IB*) force term, and to the density-based (*2phase IB*) solver. Curves on the right refer to the coarse mesh (20 cells along w_{bar}) and correspond to the pressure-based with non-linearised force term, for linear and Wallis model.

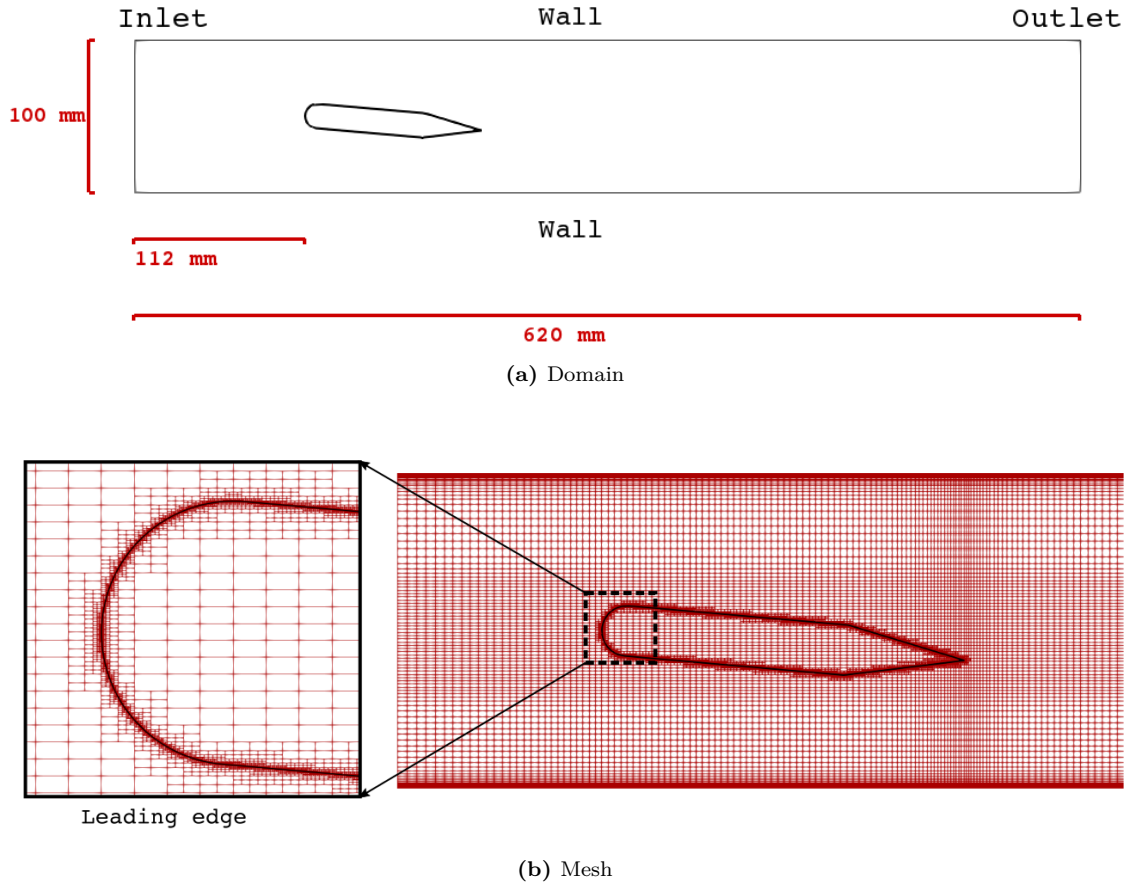


Figure 22: Computational domain (*top*) and mesh with telescopic refinement (*bottom*) for the cavitating flow over the *CLE* hydrofoil in channel. A closer look on the leading-edge of the hydrofoil is shown at the left of frame (b).

almost $U_y = 0m/s$ from 20 mm to 60 mm and start to decrease slowly. This small deviation on the cross-stream direction indicates that the proposed IB method produces a thicker boundary layer or longer cavity on average, as recirculation is pushed further towards the trailing edge.

Overall the numerical results of the current numerical approach show good agreement with the experimental measurements.

3.6 Cavitating Flow over Pitching Hydrofoil in channel

Another indicative turbulent cavitating flow test-case, of increased complexity, is the flow over a pitching NACA0066 hydrofoil at $Re = 750000$ studied numerically and experimentally by Huang et al. [4].

In the aforementioned study, a NACA0066, with chord length $c = 0.15\text{ m}$, is put in a hydraulic channel, where water

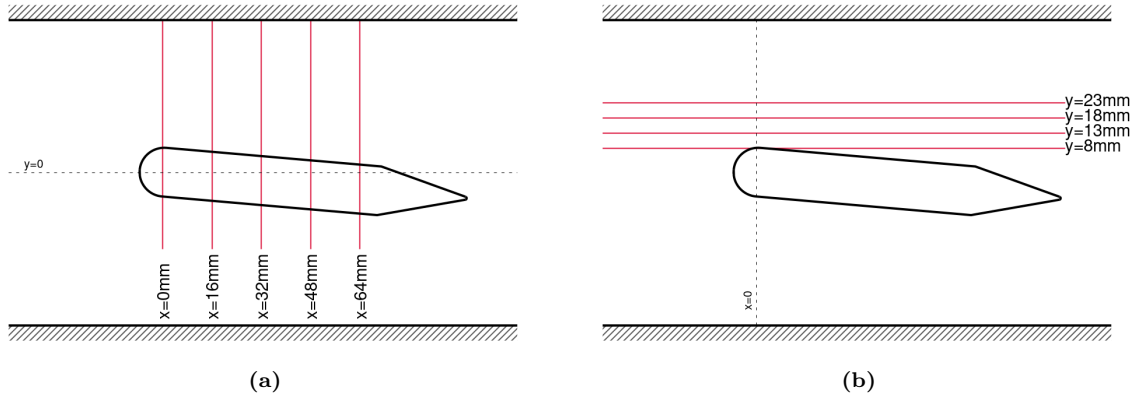


Figure 23: Sections where velocity is sampled for the flow over *CLE* hydrofoil according to [79].

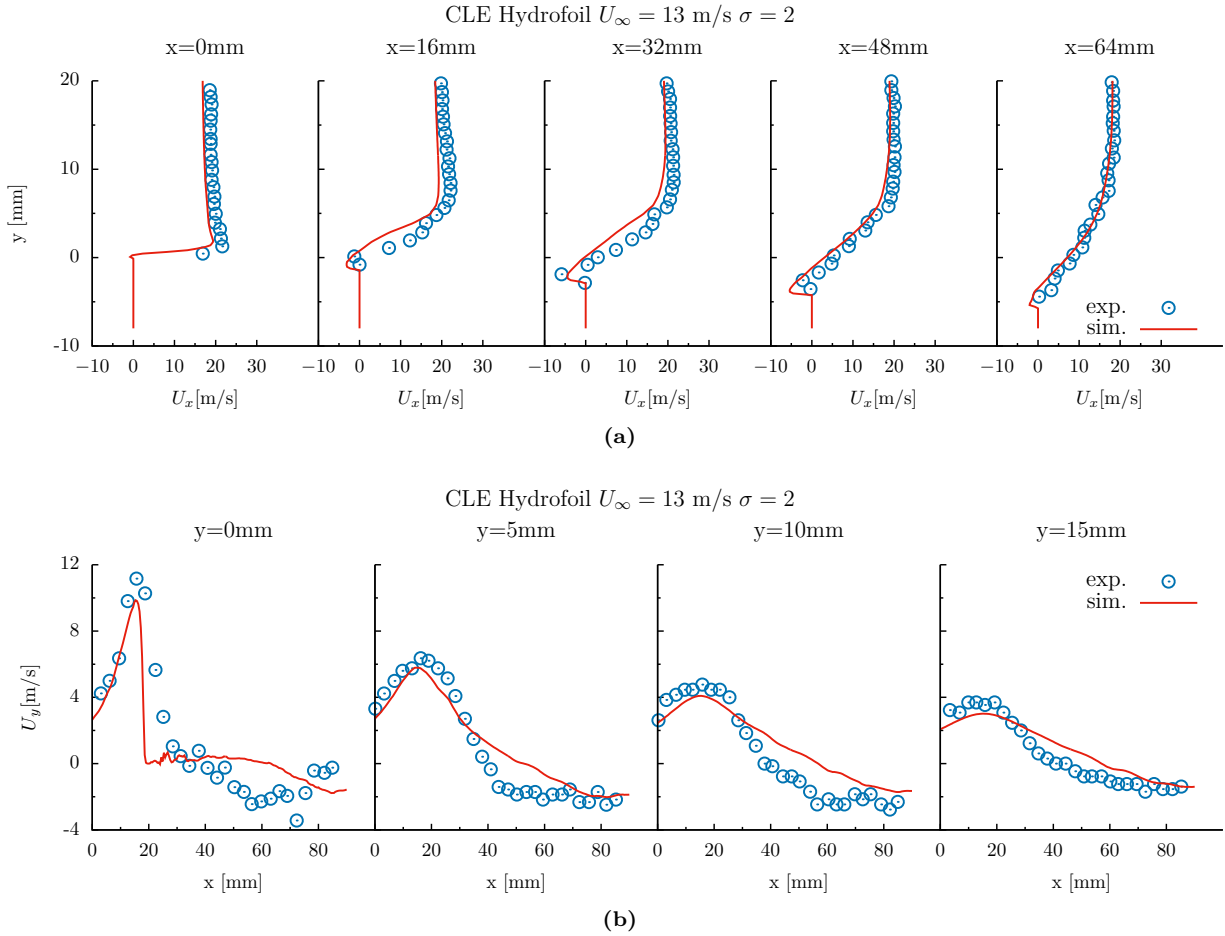


Figure 24: Time-averaged velocity profiles on different positions along stream (*top*) and cross-stream (*bottom*) directions for cavitating flow over *CLE* hydrofoil. Numerical results with the current IB method, plotted with continuous lines, are compared against experimental data from Dular et al. [79], presented with symbols.

flows at $U_\infty = 5 \text{ m/s}$ and set to rotate changing the angle-of-attack of the flow from $\alpha_{min} = 0^\circ$ to $\alpha_{max} = 15^\circ$ and back, for two different cavitating regimes (cavitating $\sigma = 3$, subcavitating $\sigma = 8$), at two different angular velocities $\dot{\alpha}^* = 0.18$ and $\dot{\alpha}^* = 1.89$, where the nondimensional rate is calculated as $\dot{\alpha}^* = \dot{\alpha} \cdot c/U_\infty$. The current study focuses only on the cavitating case with the fast pitching rate; the rotation angle is prescribed and follows the curve reported in the referenced article [4], which is shown in figure 25b and passed to the code in the form of tabulated data.

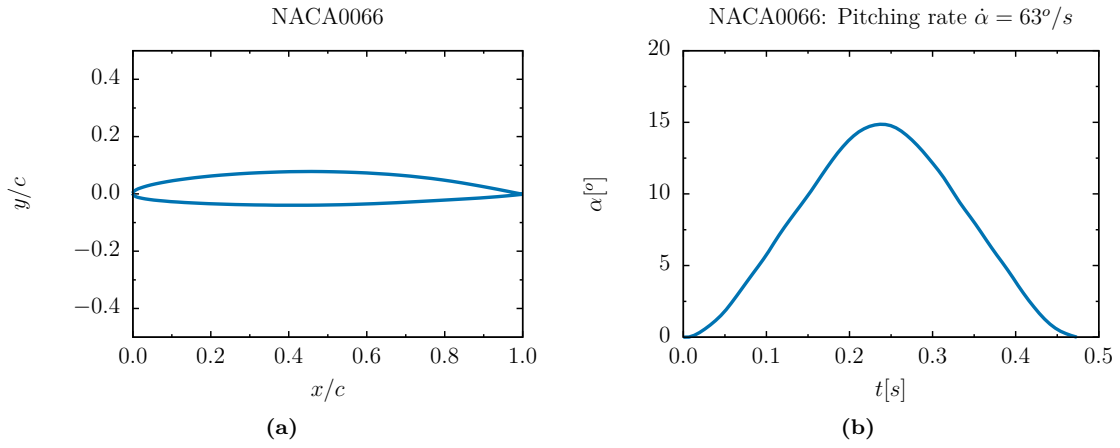


Figure 25: *Left:* The *NACA0066mod* cambered hydrofoil’s profile used in the study, extracted from the paper of Leroux et al. [80]. Maximum thickness 12% of the chord. *Right:* The prescribed rotation angle evolution through time as extracted from the paper of Huang et al. [4].

The computational domain is chosen $16c$ long and $1.28c$ high, in accordance with the computations of Huang et al. [4]. As boundary conditions, the far-field velocity U_∞ is imposed at the inlet at the left of the domain, the value of pressure p_∞ is kept constant at the outlet in order to satisfy the condition of the cavitation number $\sigma = (p_\infty - p_{vap})/(\rho U_\infty^2/2) = 3$. Moreover, following the reference study, at the top and bottom sides a *symmetry* boundary condition is set. The domain is discretised by an orthogonal hexahedral grid and telescopic refinement is used in order to increase the mesh density around the hydrofoil and its wake. Both the domain and mesh can be seen in figure 26.

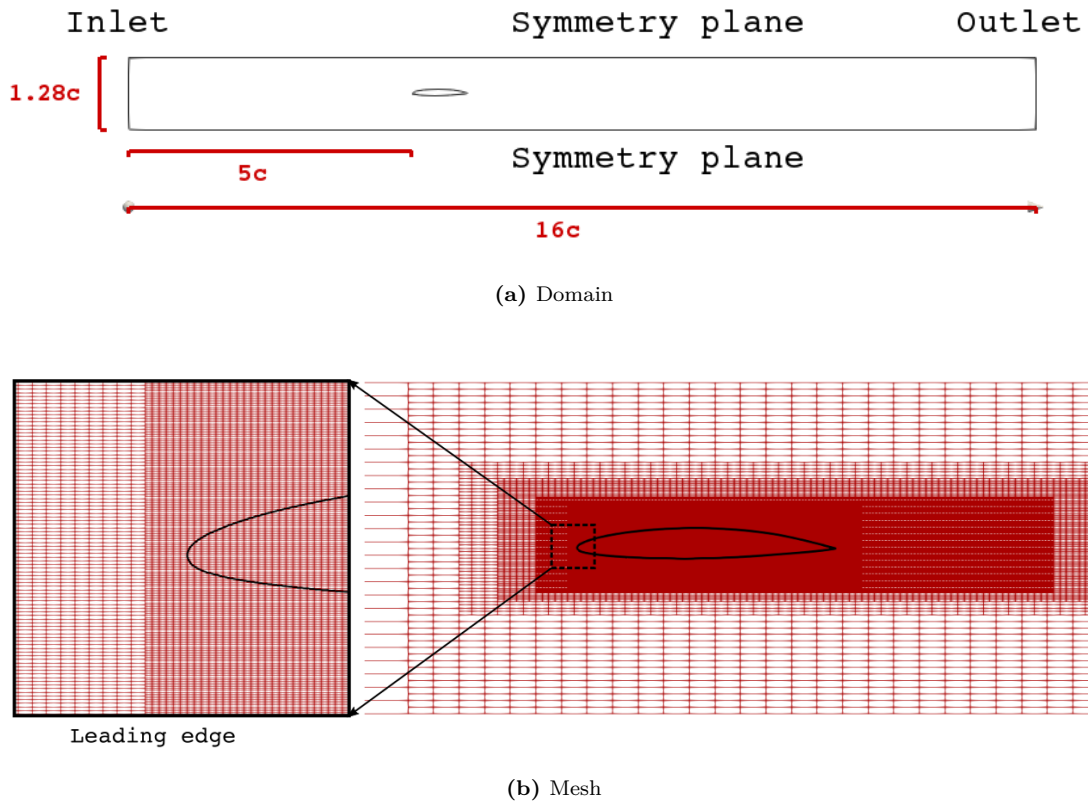


Figure 26: Computational domain (*top*) and mesh with telescopic refinement (*bottom*) for the cavitating flow over the pitching *NACA0066*. A closer look on the leading-edge of the hydrofoil is shown at the left of frame (b). The cells at the finest region, in the vicinity of the hydrofoil, have a height equivalent of $y^+ = 20$.

Using telescopic box refinement, the finest cell size reached, in an area around the NACA, is $0.47mm \times 0.12mm$, which, if the mesh was conforming to the hydrofoil’s wall, would correspond to $y^+ = 20$. In order to always have a fine grid at the interface of the immersed body, while the hydrofoil is moving, the cell size has to be kept constant in a broad area covering the path of the immersed body motion. An alternative practice would be to use a technique of automatic mesh refinement at the interface or the area of the immersed boundary, but it is out of the scope of the current study.

When using an Immersed Boundary approach, it is not trivial to determine the height of the first cell over the (immersed) wall, as the grid does not conform to the solid wall and the normal to the boundary direction does not

coincide with the cell edges. Therefore the y^+ serves rather as an indication of the grid resolution than an absolute characteristic measure of the turbulent modelling.

In their numerical computations, Huang et al. [4], use a tetrahedral grid with additional hexahedral layers over the hydrofoil's wall to capture the boundary layer. The layers ensure a mesh resolution of $y^+ = 1$ on the wall to accommodate the turbulent modelling. The computational domain is re-meshed in every time-step, to adapt to the new position of the hydrofoil. This approach of re-generation of the computational grid to deal with moving boundaries, may increase the computational cost, especially for complex geometries, and serves as a motivation for alternative techniques as the proposed Immersed Boundary.

Because of the severe transient nature of the flow, with the hydrofoil pitching past its stall-point, at an angle of $\alpha_{stall} = 13^\circ$, laminar to turbulent separation is expected to occur. For that reason, Huang et al. [4] make use of the $k - \omega$ *SSTLM* turbulence model, which is a combination of the transition model $\gamma - Re_\theta$ and the well-known low-Reynold $k - \omega$ *SST* model. They employ the *Reboud* correction for multiphase flows, which reduces the turbulent viscosity according to the local vapour volume fraction; they follow the modifications of Ducoin et al. [48] and set the value of the exponent n equal to 3 instead of 10 that was recommended by Coutier-Delgosha et al. [60] and is also used herein for equation 2.12. When using the $\gamma - Re_\theta$ model in order to accurately capture the laminar to turbulent transition, the grid cell size should yield $y^+ \simeq 1$, while for $y^+ > 5$ the transition location would be erroneously determined and moved upstream, according to Menter et al. [81]. For this reason, in the computations of Huang et al. [4], the mesh resolution ensures $y^+ = 1$ over the hydrofoil wall.

In the present study however, achieving $y^+ = 1$ near the Immersed Boundary is computationally prohibiting because a wide area would require such a fine resolution, as explained in the previous paragraphs. Therefore, different turbulence models have been employed in an attempt to alleviate the uncertainties related to fully resolving the boundary layer over the immersed wall and capturing the laminar to turbulent transition. Apart from the $k - \omega$ *SSTLM* model, the one-equation Spalart Allmaras and the low-Reynolds $k - \omega$ *SST* models have been used. The first model solves two additional, compared to the $k - \omega$ *SST*, equations for the intermittency γ and the transition momentum thickness Reynolds number Re_θ to estimate the position of the turbulent transition; it is used because it is chosen for the numerical study of Huang et al. [4]. The second model, Spalart Allmaras, is widely used in external aerodynamic flows over airfoils and solves for a single turbulent variable, the turbulent viscosity ν_t ; it is chosen for its simplicity. Finally, the $k - \omega$ *SST* is also used, because it is one of the most widely applied models on problems of engineering interest. All the models incorporate the *Reboud* correction, to account for mixture effects on the turbulent viscosity.

Figure 27 presents the off-plane vorticity field for the three different turbulence models, at various indicative angles along the pitching cycle. Differences between the predicted vorticity are visible mainly during descending phase. The 50% vapour volume fraction iso-line is also plotted to indicate the cavitation regions. Although initially small counter rotating vortices are shed in high-frequency from the trailing edge and a separation region forms and grows over the leading edge, during descending motion strong separation occurs and large vortices are shed from the leading and the trailing edges. The close relation between vorticity and cavitation is evident. Cavities are initiated, grown and carried away by vortical structures generated on the leading and trailing edges of the hydrofoil. The interaction between leading edge cavities and trailing edge vortices, highlighted in [4], is captured by all the models. The trailing edge vortices, grow until they interact with vapour structures shed over the hydrofoil from the leading edge and then get separated and carried away in the wake. This interaction also brakes down the leading edge cavities. The large vortex shedding cycles seem to be similar for the three models, but the results of the $k - \omega$ *SSTLM* show more frequent separation of smaller vortices, along with small vapour cavities, from the leading edge. On the other hand, the other models predict more steady cavities that stay attached for longer.

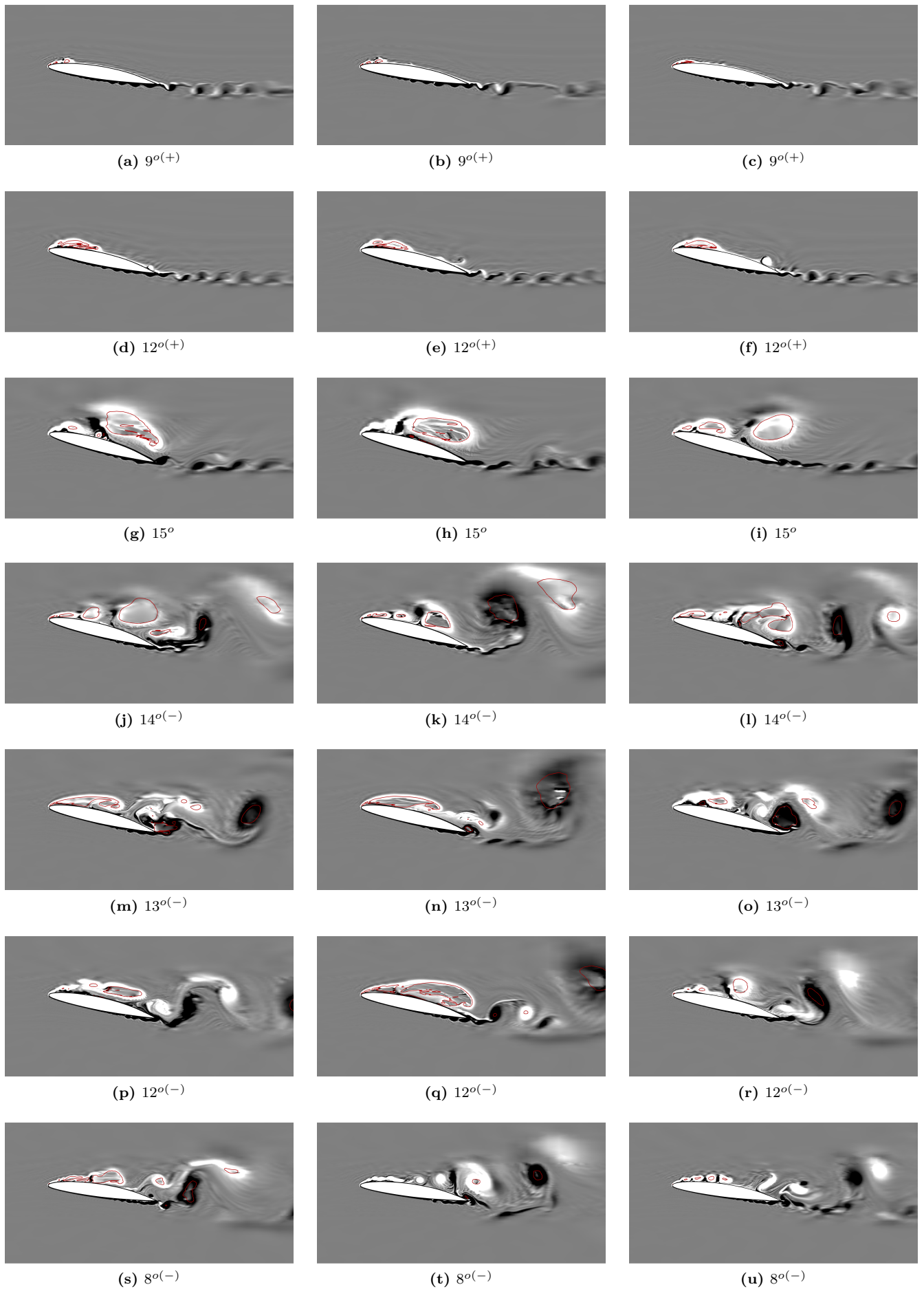


Figure 27: Vorticity field for pitching NACA0066, on different angles of attack, for the different turbulence models. Spalart-Allmaras on the *left*, $k - \omega$ SST on the *middle*, $k - \omega$ SSTLM on the *right*. The 50% vapour volume fraction iso-contour is coloured with red and the contour levels follow a reverse gray scale, from -500 (white) to $+500$ (black).

The influence of the turbulence model on the vapour creation cycle is also illustrated quantitatively by figure 28, which presents the integral vapour volume fraction evolution along the pitching motion, for the three models. Vapour generation initiates during ascending motion around $9^\circ - 10^\circ$ for all the simulations and the total vapour volume progressively increases up to pick angle, while during descending motion vapour volume formation cycles are visible, which correspond to the shedding cycles identified by the frames of figure 27. A striking difference constitutes the fact that vapour generation during descending phase is almost completely suppressed when $k - \omega SSTLM$ is used, while $k - \omega SST$ and Spalart Allmaras models capture four generation cycles. This is consistent with the observation of elongated attached cavities for the latter two models, in contrast with the shedding of small cavities from the leading edge for the $k - \omega SSTLM$. Although turbulent transition dynamics is hard and non-trivial to capture with this configuration, the $\gamma - Re_\theta$ system of equation seem to enhance the separation. From the three different models, $k - \omega SST$ exhibits the higher maximum vapour volume value shortly after pick angle is reached, while it also exhibits the faster decay during descending phase; better agreement is found among the results of the two other models between 10° ascending and 10° descending.

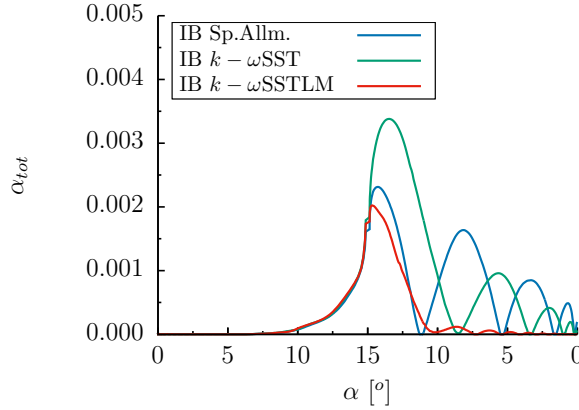


Figure 28: Integral vapour volume fraction for pitching NACA0066; comparison of simulation results with different turbulence models.

A qualitative assessment of the current computations is performed in figure 29, which presents experimental photographs and numerical vapour and vorticity fields provided by [4], along with the vorticity field and vapour iso-lines of the current numerical simulation with $k - \omega SSTLM$ model. The referenced photographs indicate the vapour cavities over the hydrofoil; good agreement among the computational and experimental results is found for the ascending phase. At 14.6° ascending, a large cavity, already detached, expands downstream the mid-cord of the hydrofoil, which is also captured by the current simulation; however the predicted cavity shape, as well as the vorticity contours, are irregular and differ from the referenced numerical results. At 14.8° descending, the referenced computational vapour field features two intense large well organised cavities over the hydrofoil towards and adjacent to the trailing edge, visible in frame 29g; these cavities are in the same position as two large counter-rotating vortices, one originated from the leading edge and one generated on the trailing edge (*Trailing Edge Vortex - TEV*). The current simulation also captures the TEV at the same angle of attack, while the vortical and vapour structures over the hydrofoil are again more irregular. These discrepancies could be attributed to the coarser grid used in the current IB calculations, in addition to a slight phase lag in the vortical and vapour dynamics. Finally, on later stages of the descending phase, the referenced flow field is smoother than the result of the current simulations, which features many small cavities in the core of small vortices on the suction side and small vortices near the trailing edge on the pressure side.

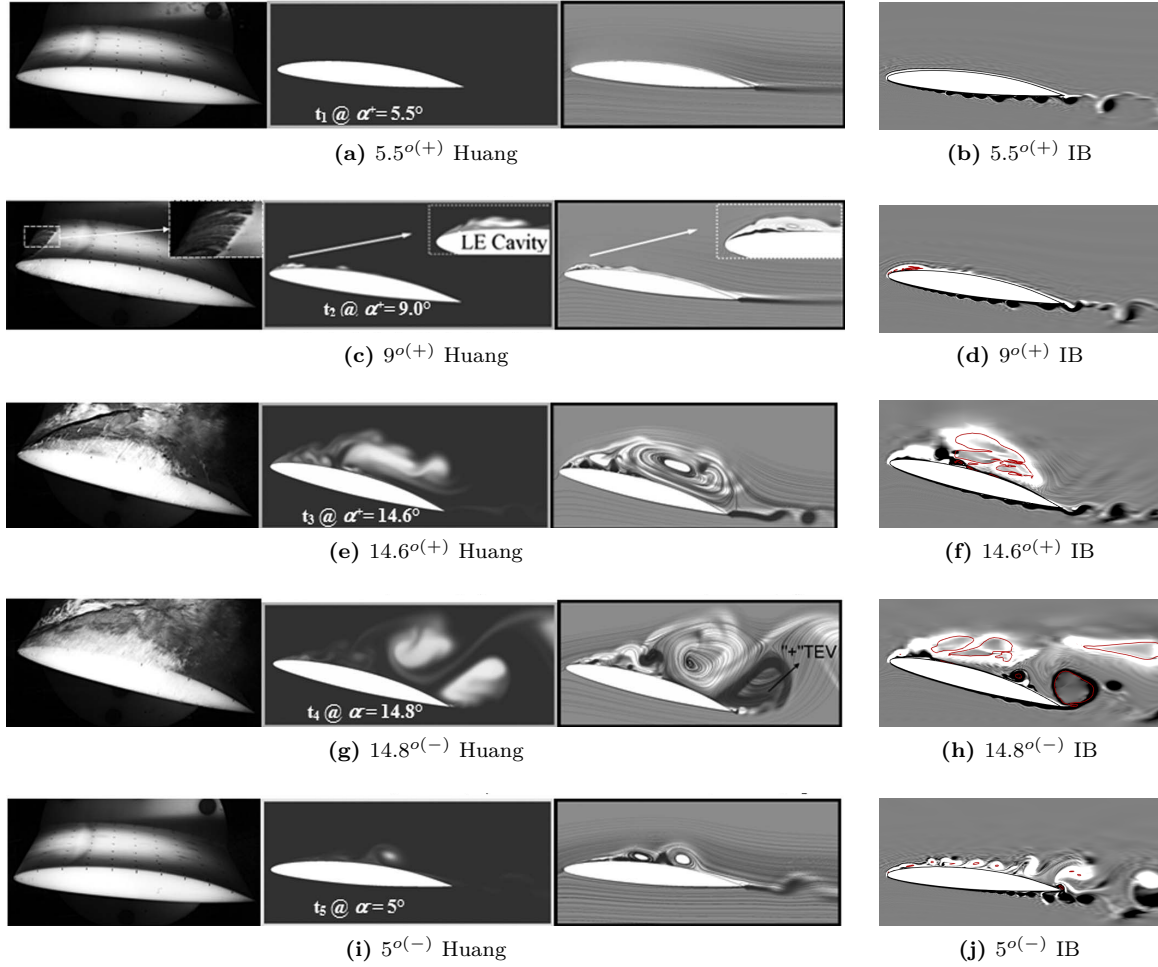


Figure 29: Vorticity field and vapour volume fraction for pitching NACA0066 calculated by the current IB methodology (*right*), compared against computational plots and experimental photographs of Huang et al. [4] (*left*). For the referenced figures of [4], experimental photographs, vapour volume fraction and vorticity field are presented from left to right respectively. On the numerical results of IB simulations (right column), the vapour volume fraction is represented by means of 50% iso-contour by the red line. On the referenced figure, the vapour volume fraction is presented on gray scale, with values ranging from 0 (black) to 0.8 (white), while vorticity is presented on reverse gray scale, from -500 (white) to $+500$ (black).

A straightforward quantitative measure of the performance of the herein proposed computational approach, would be the force coefficients' evolution throughout the rotation cycle. In figure 30, the lift, C_L , and drag, C_D , coefficients are presented for all three turbulent models used. In addition, the plots compare the current simulations' results to numerical results using conformal grid reported by Huang et al. [4], employing $k - \omega$ SSTLM; experimental values of the lift, measured for the subcavitating flow over a static hydrofoil, are also shown. It has to be noted that these available experimental lift measurements, regard a completely different flow regime from the one developed over a moving hydrofoil, cover a range of angles far below the stall point of the hydrofoil, and therefore the comparison to the numerical results can be only indicative. Because the force coefficients of the current simulations exhibit severe oscillations with frequent high amplitude spikes, they are presented by means of moving average, to ease the comparison with referenced data. These oscillations, although they could be partly comprised by numerical noise, as discussed later on this section, they also represent compressibility effects; the reported computation of Huang et al. is incompressible therefore pressure waves are not captured and the resulting body forces have a rather smooth profile. It can be seen that, while ascending, the curves for all IB computations agree well with the referenced computations; some noise is present in both drag and lift coefficients for all the simulations. During the descending motion, the three IB computations diverge; $k - \omega$ SSTLM constantly over-predicts the drag, as well as the lift in most part of the descending phase; the results of Spalart Allmaras seem to be closer to the referenced data, however they exhibit strong persistent increases and decreases and therefore diverge. The results of the $k - \omega$ SSTLM model, in spite of the clear deviation and almost constant over-prediction of the forces, they seem to capture similar dynamics found in the referenced computations; the evolution of the coefficients' curves have similar increases and decreases, however the current simulations follow with a small delay.

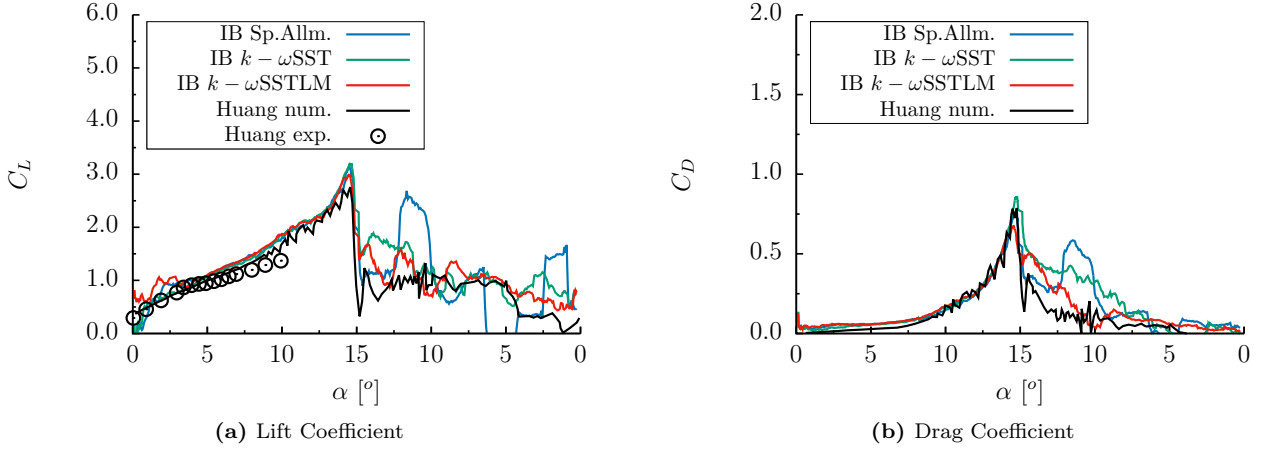


Figure 30: Centered Moving Average (*CMA*) trend-lines of force coefficients for pitching NACA0066; comparison of simulation results with different turbulence models. Numerical and experimental results of Huang et al. [4] are also presented; continuous black line refers to transient computations of cavitating pitching hydrofoil, while the black symbols are static lift measurements for fixed subcavitating hydrofoil.

By sampling the pressure field on the surface of the hydrofoil, modelled as an immersed boundary, the pressure coefficient distribution along the sides of the foil can be determined, calculated at $C_p = 2(p - p_{\text{inf}})/(\rho_{\text{inf}}U_{\text{inf}}^2)$. In figure 31 it is plotted for different angles during the ascending phase. On the one hand, the noise of the sampled data is evident. It can be explained as a side effect of the direct forcing in conjunction with the severely transient nature of the flow, as well as the lack of special treatment for the pressure field, as it will be explained hereafter. On the other hand, a distinctive oscillatory behaviour can be observed, which partially can be related to the modelling approach but also to the very characteristics of the flow and the vortex shedding, which is initiated early in the cycle on the pressure side. Equivalent curves reported by Huang et al. [4], although they predict a very smooth profile along the pressure side of the hydrofoil, they capture a similarly distorted pressure distribution on the suction side, with peaks towards the leading edge and plateaux towards the last half; these are visible in figure 31 for angles $8^{\circ(+)}$ and 15° . There the pressure coefficient reaches the limit value of -3 which corresponds to the cavitation number and indicates the location of vapour cavity. An interesting artefact captured by the herein presented simulations, is the inversion of the curves that takes place near the trailing edge at peak angle 15° . This is related to the sudden and abrupt change in the direction of the rotation; it is linked with the stall and the TEV generation. This observation agrees with the data of the aforementioned literature, where in addition a less rapid rotation and a less violent flow are studied, for which these distortions are absent. The work of Hejranfar et al. [47], on the cavitating flow past a stationary NACA0066(MOD) hydrofoil at a low angle, in an inviscid framework, employing both barotropic and mass transfer models (transport equation-based models *TEM*), alleviate the computational uncertainties of the turbulence modelling and reduce them to the choice of empirical constants on the cavitation models. In addition, they also report severe pressure drops at the end of the cavity, which in their case remains attached. This is clearly visible near the leading edge for the curve corresponding to $8^{\circ(+)}$ in figure 31.

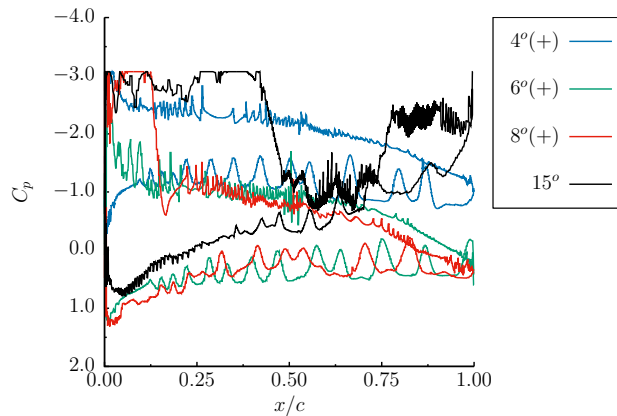


Figure 31: Pressure coefficient for pitching NACA0066, at different angles on the ascending phase. Results correspond to the use of $k - \omega SSTLM$.

It can be stated that, overall, the results of the IB and the conformal grid computations are close, despite the severe oscillations of the forces and the time-shift of the developed phenomena present in the former. Both qualitative and quantitative comparison of all the computations and the experiments, yield good if not perfect agreement for the ascending phase of the motion, while for the descending phase, the results of the IB simulations deviate from that of

the conformal grid, although it is found that, depending on the turbulence model used, the dynamics of the flow can be closely replicated. The close relation between cavitation and vortical structures is evident. The IB simulations are limited by grid resolution that prevents them from accurately capturing stall and transition to turbulence in the boundary layer over the hydrofoil wall. The use of an automatic mesh refinement method, could ensure the fine grid resolution in the vicinity of the immersed body interface, and therefore enhance the performance of the turbulence models, while keeping the mesh size reasonable and the computational cost low. In addition, the difference in cavitation modelling may play a role for these discrepancies, although probably small; the simulations of Huang et al. [4] employ a homogeneous mixture model coupled with Merkle mass-transfer model for phase change, while the current IB simulations follow a HEM approach coupled with a barotropic EOS. According to the rationale of Huang et al., the barotropic approach was avoided because it would not be able to capture the baroclinic torque, i.e. the miss-alignment of the pressure and density gradients, which is thought to play a significant role in cavitation initiation. However there is no proof that mass transfer models can predict the correct baroclinic torque either. Moreover, the parametric computational study of the cavitating flow over a NACA0066(MOD) reported by Hejranfar et al. [47], showed that very good agreement can be achieved between barotropic and mass transfer approaches, with the latter to be sensitive in the choice of their empirical coefficients. In conclusion, the herein proposed method proved adequate in treating this complex case and capturing the reported physics, although room for improvement exists.

Moreover, regarding the treatment of the IB source term, the influence of the linearisation of the forcing term is studied in figure 32. It can be seen that although the oscillatory nature of the curves has not vanished, the high-amplitude spikes have been drastically reduced. This confirms that these oscillations are partly caused by the numerical method or the discretisation employed, however since compressibility is taken into account, pressure waves and therefore noise on the body forces are expected. The pressure field is let to naturally evolve inside the immersed body, influenced only by the momentum forcing term imposing the no-slip condition, therefore an additional source term enforcing a pressure boundary condition, as the one proposed by Riahi et al. [20] for compressible flows, as well as finer spatial resolution near the body interface, as discussed previously, could further improve the results; however all these numerical enhancements would not completely remove the noise from the body forces, which is linked to the highly transient nature of compressible effects of cavitating flows. In addition, it is evident that the simulations with the $k - \omega$ *SSTLM* model produce the results closest to the reference computations of Huang et al. [4], which employ the same turbulence model.

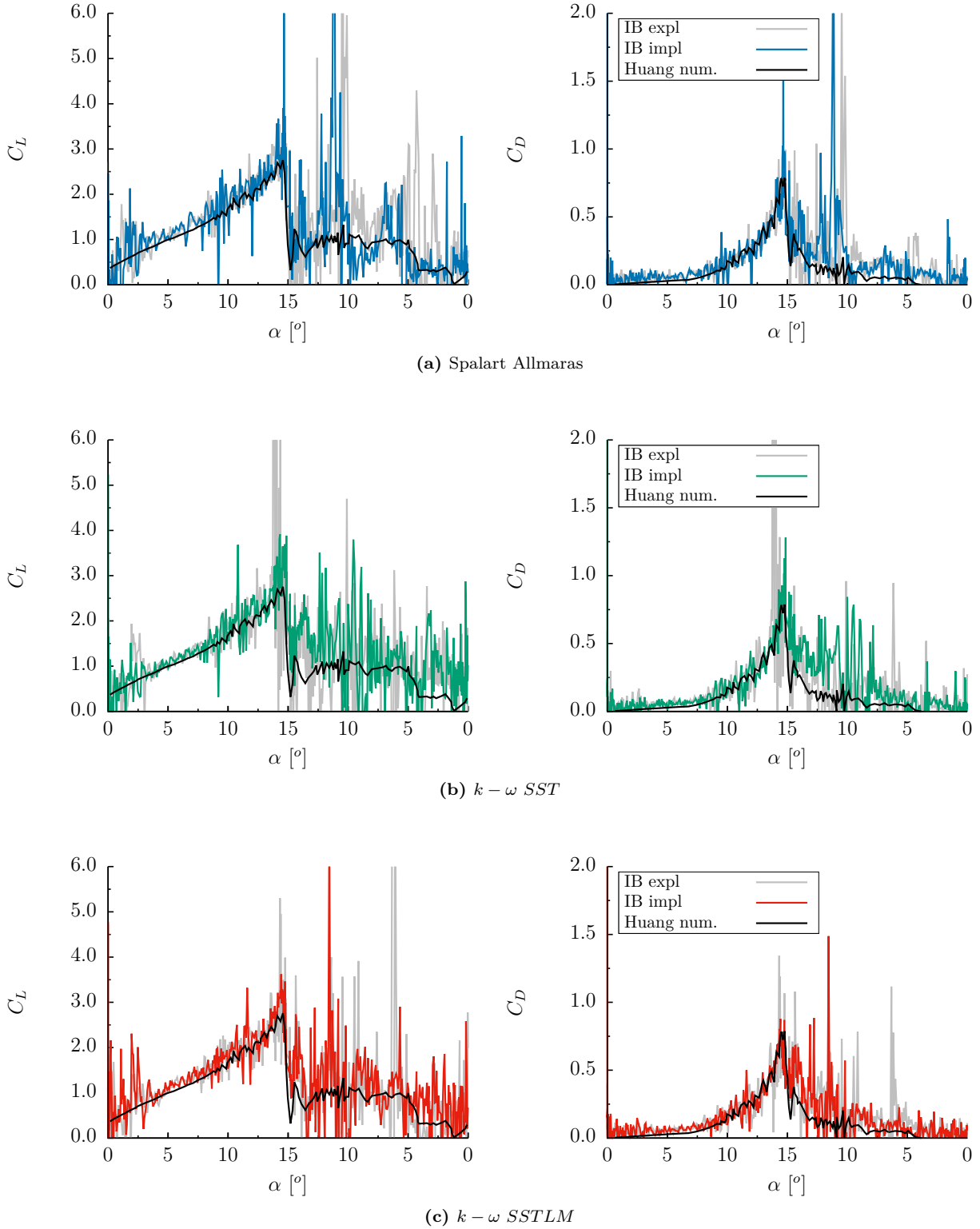


Figure 32: Force coefficients for pitching NACA0066; comparison of simulation results with explicit and implicit treatment of the forcing source term, for different turbulence models. Numerical results of Huang et al. [4] are also presented.

Finally, with regards to the computational time, it has to be noted that although the simulations demanded significant computational resources and were rather long, this was a result of the long simulated time interval ($0 - 0.47s$) and the small time-step ($dt_{mean} = 1.29 \cdot 10^{-7}s$) dictated by the cavitating regime. It has to be highlighted that the computational cost stems from the requirements on the flow solver, as the motion of the hydrofoil is accommodated by the IB, without alternation of the mesh; this does not add additional computational burden. More precisely, for the simulation of the ascending motion of the pitching NACA0066 with Spalart-Allmaras turbulence model, for approximately $0.23s$, the computational cost was $2414cpuh$ on 8 cores of a workstation equipped with an Intel Xeon E5-2690 V3 @ $2.6GHz$ processor. For the simulation of the turbulent cavitating flow over the same stationary hydrofoil, for $0.2s$, using the same turbulent model, $2238cpuh$ were required. Thus, it can be seen that the IB method has a significant advantage over any adaptive conformal grid technique.

3.7 Cavitation in a Diesel Injector with needle movement

Finally, in this section, a pilot injection, dwell time, and subsequent start of the injection cycle of a Diesel Injector are simulated considering the needle valve movement. This is an indicative case of industrial application, demonstrating the ability of the proposed IB Method to deal with complex cavitating turbulent flows.

The IB methodology is particularly relevant for these cases as it allows the modelling of the flow field at zero lift, where the needle remains closed. Numerous numerical works are focused on these flows, which accommodate the movement with either complete re-meshing the domain [4] or cell layer addition and inflation [5] or interpolating between grids of different resolution but same cell count [82]; only few studies employ cut-cell IB methods [32–36], which however do not permit the needle to fully close but rather demand a minimum lift of about 8% [32], 2%-4% [33] or 1.5% [34]. Cut-cell methods could be an alternative option, though the cartesian background geometry would necessitate an excessive amount of cells for describing small needle/needle seat gaps. An accurate simulation of the needle movement, including full-closed position, is essential to capture the pressure-wave dynamics and the residual fuel remaining in the injector’s sac volume between successive injection events, a phenomena that plays a major role in nozzle wall wetting and emissions, as demonstrated by a recent work of the author’s group [41].

The geometry employed is a 6-hole valve covered orifice (VCO). The computational domain, as well as a general and a detailed view of the mesh are visible in figure 34. The computational domain covers the injector and the combustion chamber in the vicinity of the nozzle exit. The VCO is initialized with 100% Diesel at 1600bar, except for the orifices that are initialized at 40bar. The combustion chamber is initialized with 100% air at 40bar and 700K. A constant pressure of 1600 bars and 40 bars is applied at the inlet and outlet boundaries, respectively.

For this simulation, the density-based solver is employed, which uses 10^3 times smaller steps compared to the previously simulated cases [41], where a pressure-based solver was used, and thus, better captures the dynamic effects linked with the residual fuel inside the nozzle’s sac volume and injection hole during the dwelt time. Moreover, although recent studies [83–85] consider temperature effects, for the cases examined here, that refers to pilot injection at a rail pressure of 1600, temperature effects can be ignored [86–90]. The Diesel properties employed in the simulations are the ones considered in the aforementioned study [41]. The air properties were computed using the NIST (REFPROP) library [91]. Regarding the turbulence, instead of RANS a LES approach is employed and the turbulent viscosity is modelled using the Wall Adaptive Large Eddy (WALE) method [92]. In contrast to the RANS simulations, wall distance adaptation is not taken into account by the LES model. Figure 33 shows the needle lift employed in the simulation and the mass flow rate per orifice. The observations and obtained results agree with that of the previously published study [41].

VCO Diesel Injector: Needle lift and mass flow rate

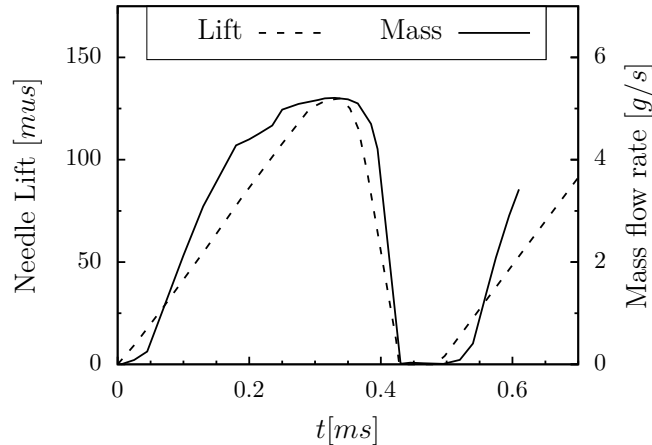


Figure 33: VCO Diesel Injector’s simulation imposed needle lift and calculated mass flow rate

The evolution of the cycle and the two distinct cavitation formation mechanism are illustrated in figures 35 for the Start of Injection Transients (*SOI*) and 36 for the End of Injection (*EOI*). At the start of the first injection, a small amount of air from the combustion chamber is suctioned into the orifices and at $32\mu m$ lift, geometric-induced cavitation is initiated at the inlet edge due to the high flow speed generated between the needle and nozzle walls, as it is illustrated in the time-instances of figure 35. On the other hand, during the closure, as the needle valve approaches its seat, the pressure near the needle drops to values lower than the saturation pressure of Diesel, resulting in localized cavitation near the inlet of the orifices (figure 36b). These cavitation pockets are elongated towards the exit of the orifices during the last stages of the needle closure (figures 36d, 36e, 36f), and when the needle reaches $0\mu m$ lift (figure 36g), an effect like inverse water hammer takes place. Once the fuel has lost its momentum, the increased pressure in the combustion chamber pushes the Diesel and air from the chamber toward the inlet of the orifices, collapsing the vapor cavities (figures 36h, 36i) leading to air ingestion. The existence of gas voids within the orifices before the start of the injection was observed experimentally [93] with the visualization of a sack-type injector and is of importance in quantifying realistic initial conditions for spray simulations. The geometric cavitation inside the orifices in the second injection, is significantly lower than in the first one due to expansion of the gas present inside the orifice when the pressure drops, as it can be seen in the time-instances of Subsequent Start of Injection (*SSOI*) in figure 37.

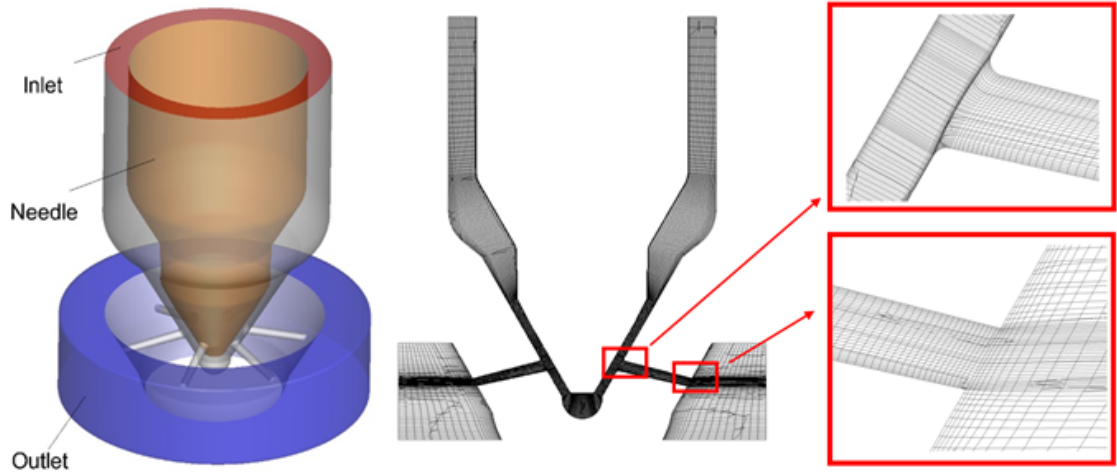


Figure 34: (a)VCO geometry, (b)cross-section of the hexahedral mesh employed, (c)mesh details near orifice entrance and exit.

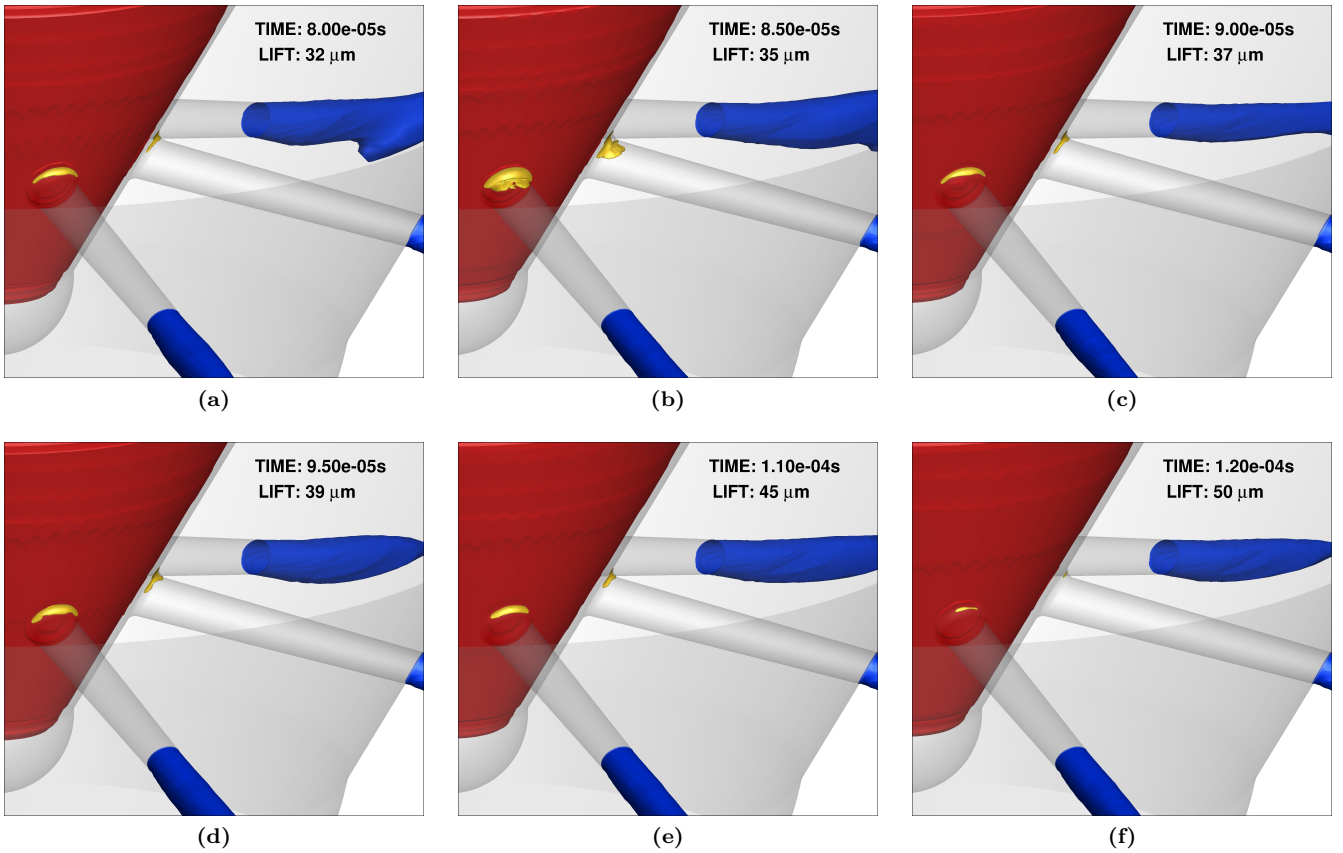


Figure 35: Geometric cavitation formation during opening of Diesel injector needle valve (SOI). Iso-surfaces of IB mask $\alpha_{IB} = 0.99$ (red), 20% vapour volume fraction (yellow), and 5% gas mass fraction (blue).

4 Conclusions

In the current paper a direct forcing Immersed Boundary method has been proposed for complex turbulent cavitating flows, involving moving boundaries.

The proposed methodology, follows a direct forcing approach and introduces a forcing source term in the momentum equations to account for the presence of the immersed body in the fluid. The source term is localised on all cells covered by the solid surface representing the immersed body by using a continuous mask. Thus, it overcomes the *stair-case* issue on interface cells, avoids the cumbersome interpolation procedure, the definition of every intersection of the geometrical representation of the body with the computational grid or the sophisticated sub-grid reconstruction of the boundary, present in other Immersed Boundary methods and therefore, profits from simplicity in its formulation.

In addition, compared to other alternatives, the method poses as a simpler and more cost-effective computational approach for complex flows in domains of changing geometry. The significantly lower computational in comparison with sliding conforming grids approach and the simpler and less complex algorithm than the re-meshing techniques, are important advantages. The has been applied to turbulent cavitating flows involving moving boundaries, characterised by highly transient phenomena, for which the computational cost of conforming grid techniques would be prohibiting.

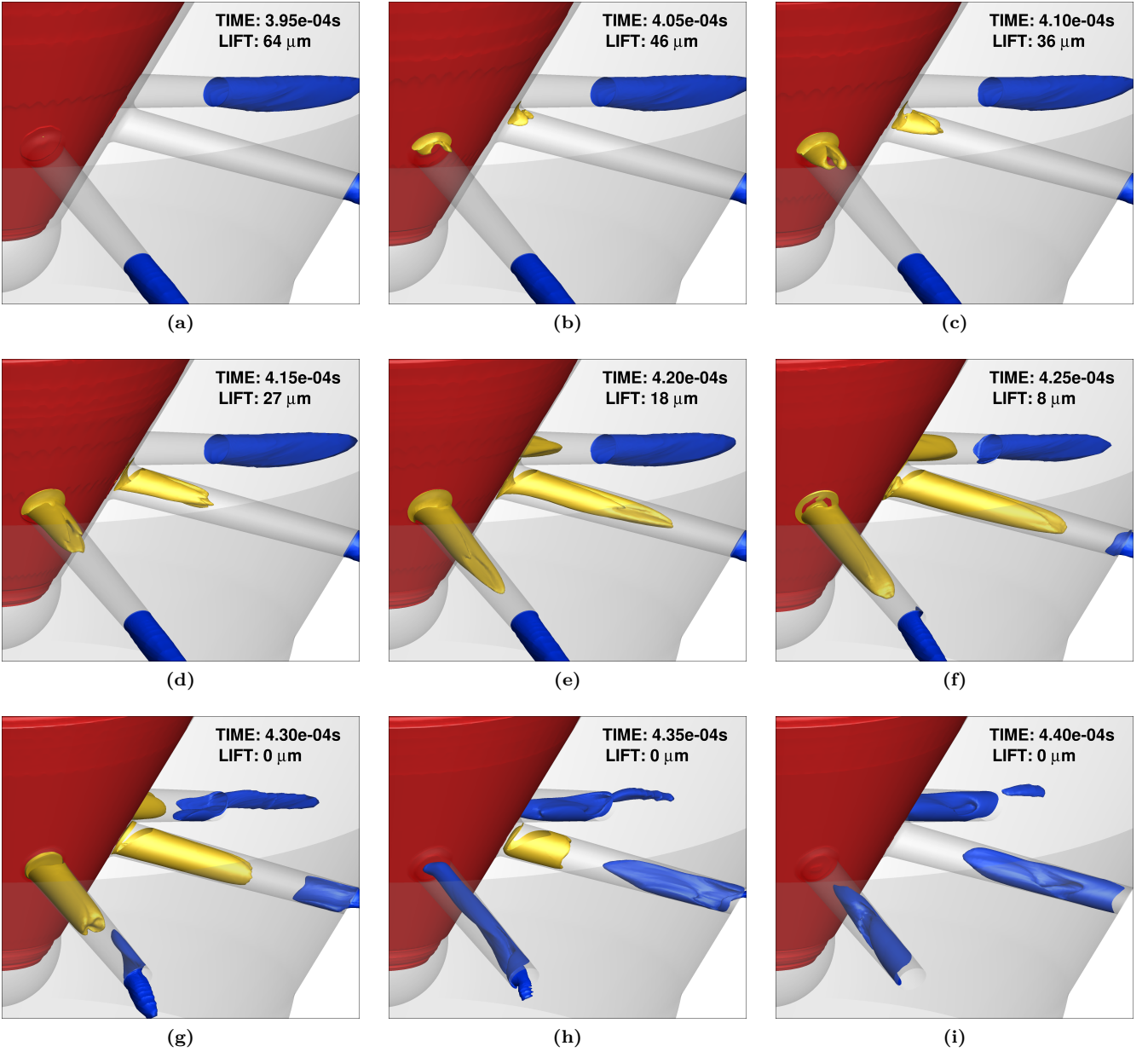


Figure 36: Collapse cavitation formation during closing of Diesel injector needle valve (EOI). Iso-surfaces of IB mask $\alpha_{IB} = 0.99$ (red), 20% vapour volume fraction (yellow), and 5% gas mass fraction (blue).

The proposed method has been validated on benchmark cases with increasing complexity, from incompressible laminar and low-Reynolds flows to compressible high-Reynolds turbulent multiphase flows with phase change. The performance of the method has been assessed against experimental data and computational results available in the open literature, as well as conformal grid simulations when possible. The results obtained with the proposed method are found in good agreement with the reference data, demonstrating that it is capable of treating complicated cavitating flows around moving bodies with satisfactory accuracy.

Acknowledgement

This work was carried out in the framework of [CaFE](#) project, which has received funding from the European Union Horizon 2020 Research and Innovation programme, with Grant Agreement No 642536.

A Accuracy of the Method

To assess the accuracy of the developed Immersed Boundary method, the *Euclidean* or L_2 norm of the velocity field error $\mathbf{e} = \mathbf{u} - \mathbf{u}_{ref}$ is used to quantify the dependency of the computational error from the spatial resolution. The error is evaluated as the volume-weighted average of the square of its norm by the relation [A.1](#), for the cases of an oscillating

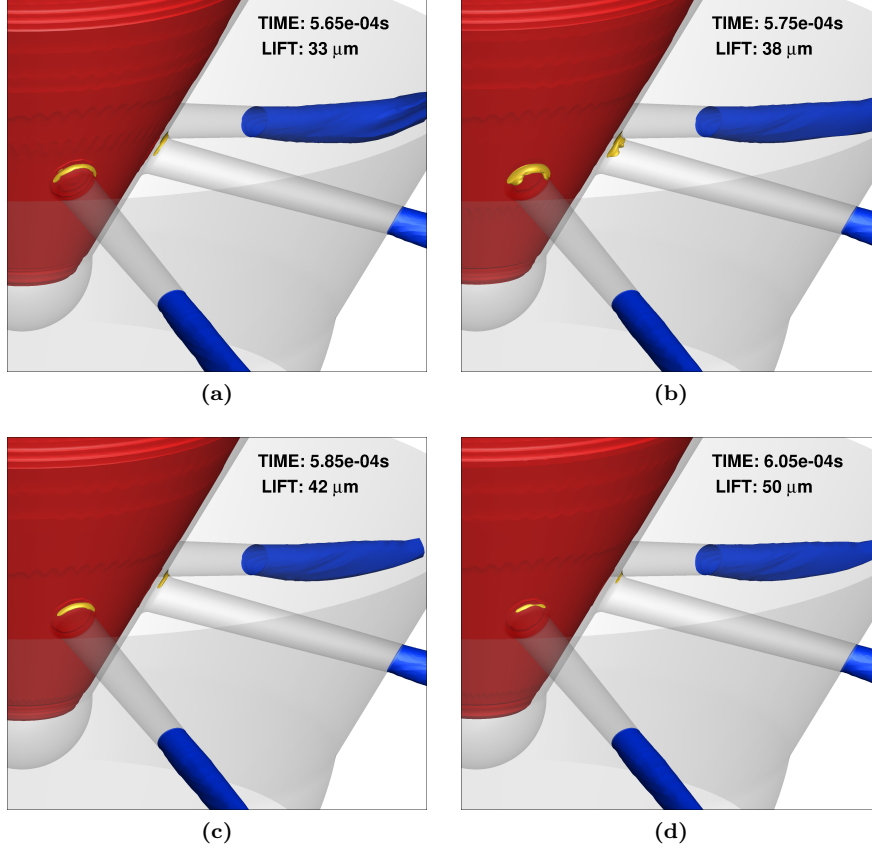


Figure 37: Geometric cavitation formation during second opening of Diesel injector needle valve (SSOI). Iso-surfaces of IB mask $\alpha_{IB} = 0.99$ (red), 20% vapour volume fraction (yellow), and 5% gas mass fraction (blue).

cylinder in stagnant fluid, of section 3.1, and the supersonic flow over a stationary cylinder, of section 3.3.

$$\|e_u\| = \|e\| = \sqrt{\frac{1}{V_T} \int \|e\|^2 dV} = \sqrt{\frac{1}{V_T} \sum_j^n V_j \|\mathbf{u}_j - \mathbf{u}_{ref,j}\|^2} \quad (\text{A.1})$$

where V_j and \mathbf{u}_j refer to the volume and velocity, respectively, of the cell j of the discretised computational domain, of total volume V_T and total cell number n . As the reference velocity field, \mathbf{u}_{ref} , is chosen in both cases the velocity field of the finest grid, thus the order of convergence rate of the velocity error with increasing spatial resolution is studied.

For the simulation of oscillating cylinder in incompressible fluid, using the pressure-based approach, in addition to the three canonical grids presented in section 3.1, namely the $5\%D_{cyl}$ (coarse), $2.5\%D_{cyl}$ (medium) and $1.25\%D_{cyl}$ (fine), yielding a total number of $67k$, $137k$ and $334k$ cells respectively, another coarser grid, of $51k$ cells, is employed with a resolution of $10\%D_{cyl}$. Similarly, for the case of compressible supersonic flow over stationary cylinder, simulated with the density-based solver, apart from the three grids mentioned in section 3.3, with resolutions of $dx = 7.4\%D_{cyl}$ (coarse), $dx = 3.7\%D_{cyl}$ (medium) and $dx = 1.9\%D_{cyl}$ (fine) in the vicinity of the cylinder, a fourth coarser grid, with $dx = 14.8\%D_{cyl}$, is used to study the convergence. The estimated errors are shown in figure 38 and suggest that the method achieves first order of accuracy; is in accordance with the findings of Fadlun et al. [16].

Another way to quantify the accuracy of the method is to examine the pressure and density field residuals, for the iterative pressure-correction and the explicit density-based algorithms, respectively. For the case of cavitation induction from the rotating cross of section 3.4, the initial and final iterations' residuals of the pressure field of the pressure-based solver coupled with the IB are compared to those of the sliding-mesh (AMI) approach in figure 39a. Although both methods achieve good convergence, for the sliding mesh the residual reaches 10 orders of magnitude lower values. The IB method clearly converge and systemically achieve residuals of the order of 10^{-9} . This is confirmed also for the case of high turbulent cavitating flow over the pitching hydrofoil presented in section 3.6, from the figure 39b. However in this case the values of the residual oscillate severely but in acceptable range. Finally, for the rotating cross case, the residual of the density-based solved is also plotted in 39a for comparison. It can be observed that although some noise exists, the residual do not exhibit these strong oscillations as of the pressure-based solver. In all cases, the IB method produces satisfactory convergence.

References

- [1] Koukouvini P, Bruecker C, Gavaises M. Unveiling the physical mechanism behind pistol shrimp cavitation. *Scientific Reports* 2017; 7(1): 13994. doi: 10.1038/s41598-017-14312-0

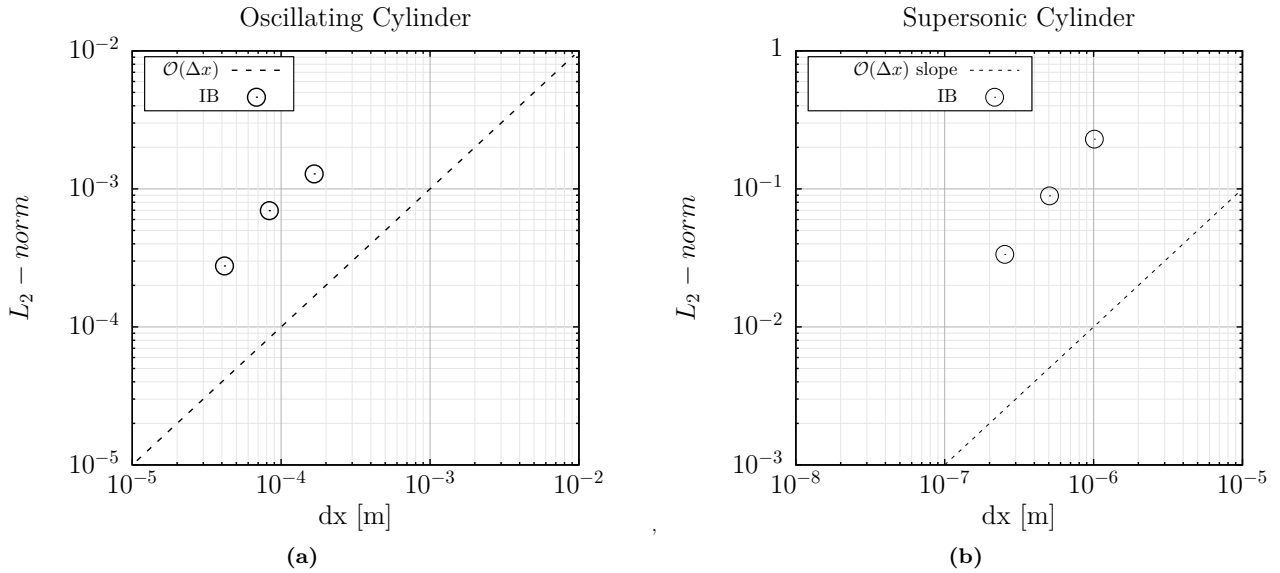


Figure 38: L_2 error norm of velocity field, of oscillating cylinder in incompressible stagnant fluid using pressure-based (a) and for the case of supersonic flow over stationary cylinder using density-based (b) algorithms.

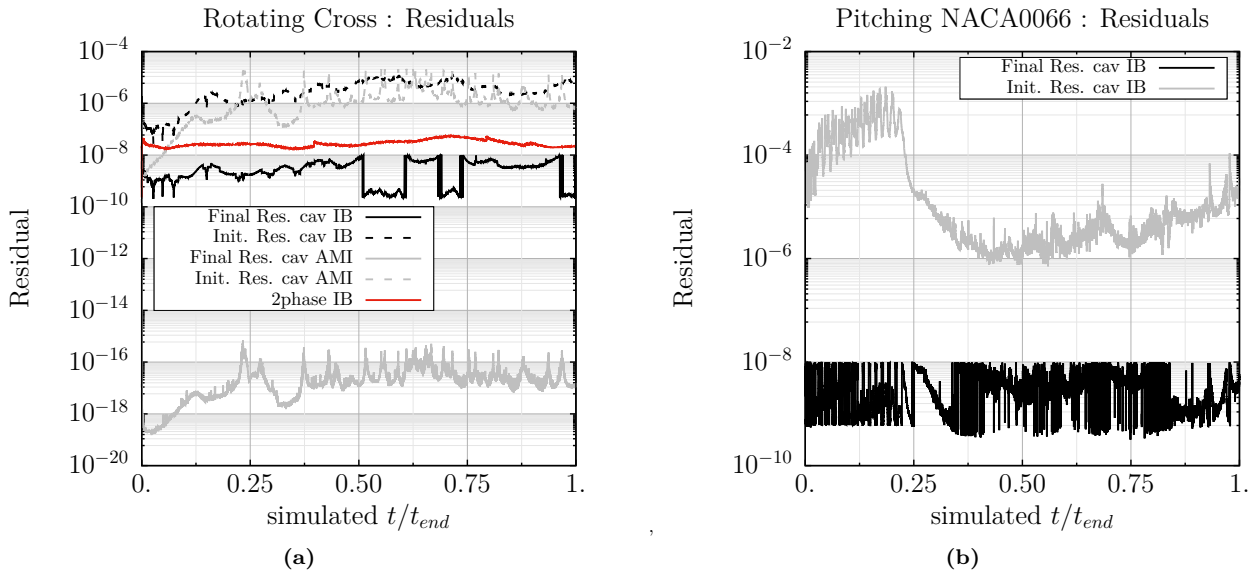


Figure 39: Pressure and density residuals for the cases of cavitation induction from a rotating cross in stagnant liquid presented in section 3.4 (a) and from the flow over a pitching hydrofoil presented in section 3.6 (b).

- [2] Stavropoulos Vasilakis E, Kyriazis N, Koukouvinis P, Farhat M, Gavaises M. Cavitation induction by projectile impacting on a water jet. *International Journal of Multiphase Flow* 2019; 114: 128–139. doi: [10.1016/j.ijmultiphaseflow.2019.03.001](https://doi.org/10.1016/j.ijmultiphaseflow.2019.03.001)
- [3] Mithun MG, Koukouvinis P, Karathanassis IK, Gavaises M. Numerical simulation of three-phase flow in an external gear pump using immersed boundary approach. *Applied Mathematical Modelling* 2019; 72: 682–699. doi: [10.1016/j.apm.2019.03.022](https://doi.org/10.1016/j.apm.2019.03.022)
- [4] Huang B, Ducoin A, Young YL. Physical and numerical investigation of cavitating flows around a pitching hydrofoil. *Physics of Fluids* 2013; 25(10): 102109. doi: [10.1063/1.4825156](https://doi.org/10.1063/1.4825156)
- [5] Koukouvinis P, Gavaises M, Li J, Wang L. Large Eddy Simulation of Diesel injector including cavitation effects and correlation to erosion damage. *Fuel* 2016; 175: 26–39. doi: [10.1016/j.fuel.2016.02.037](https://doi.org/10.1016/j.fuel.2016.02.037)
- [6] Bensow RE, Bark G. Implicit LES Predictions of the Cavitating Flow on a Propeller. *Journal of Fluids Engineering* 2010; 132(4). 041302 doi: [10.1115/1.4001342](https://doi.org/10.1115/1.4001342)
- [7] Melissaris T, Bulten N, Terwisga vT. On Cavitation Aggressiveness and Cavitation Erosion on Marine Propellers using a URANS Method. In: ASME Press. 2018

- [8] Tramel R, Nichols R, Tramel R, Nichols R. A highly efficient numerical method for overset-mesh moving-body problems. In: ; 1997: 2040.
- [9] Mittal R, Iaccarino G. Immersed Boundary Methods. *Annual Review of Fluid Mechanics* 2005; 37(1): 239–261. doi: [10.1146/annurev.fluid.37.061903.175743](https://doi.org/10.1146/annurev.fluid.37.061903.175743)
- [10] Peskin CS. Numerical analysis of blood flow in the heart. *Journal of Computational Physics* 1977; 25(3): 220–252. doi: [10.1016/0021-9991\(77\)90100-0](https://doi.org/10.1016/0021-9991(77)90100-0)
- [11] Iaccarino G, Verzicco R. Immersed boundary technique for turbulent flow simulations. *Applied Mechanics Reviews* 2003; 56(3): 331–347.
- [12] Sotiropoulos F, Yang X. Immersed boundary methods for simulating fluid–structure interaction. *Progress in Aerospace Sciences* 2014; 65: 1–21. doi: [10.1016/j.paerosci.2013.09.003](https://doi.org/10.1016/j.paerosci.2013.09.003)
- [13] Lai MC, Peskin CS. An Immersed Boundary Method with Formal Second-Order Accuracy and Reduced Numerical Viscosity. *Journal of Computational Physics* 2000; 160(2): 705–719. doi: [10.1006/jcph.2000.6483](https://doi.org/10.1006/jcph.2000.6483)
- [14] Goldstein D, Handler R, Sirovich L. Modeling a No-Slip Flow Boundary with an External Force Field. *Journal of Computational Physics* 1993; 105(2): 354–366. doi: [10.1006/jcph.1993.1081](https://doi.org/10.1006/jcph.1993.1081)
- [15] Mohd-Yusof J. Development of immersed boundary methods for complex geometries. In: Center for Turbulence Research. 1998.
- [16] Fadlun E, Verzicco R, Orlandi P, Mohd-Yusof J. Combined Immersed-Boundary Finite-Difference Methods for Three-Dimensional Complex Flow Simulations. *Journal of Computational Physics* 2000; 161(1): 35–60. doi: [10.1006/jcph.2000.6484](https://doi.org/10.1006/jcph.2000.6484)
- [17] Uhlmann M. An immersed boundary method with direct forcing for the simulation of particulate flows. *Journal of Computational Physics* 2005; 209(2): 448–476. doi: [10.1016/j.jcp.2005.03.017](https://doi.org/10.1016/j.jcp.2005.03.017)
- [18] Blais B, Lassaigne M, Goniva C, Fradette L, Bertrand F. A semi-implicit immersed boundary method and its application to viscous mixing. *Computers & Chemical Engineering* 2016; 85: 136–146. doi: [10.1016/j.compchemeng.2015.10.019](https://doi.org/10.1016/j.compchemeng.2015.10.019)
- [19] Mochel L, Weiss PÉ, Deck S. Zonal Immersed Boundary Conditions: Application to a High-Reynolds-Number Afterbody Flow. *AIAA Journal* 2014; 52(12): 2782–2794. doi: [10.2514/1.J052970](https://doi.org/10.2514/1.J052970)
- [20] Riahi H, Meldi M, Favier J, Serre E, Goncalves E. A pressure-corrected Immersed Boundary Method for the numerical simulation of compressible flows. *Journal of Computational Physics* 2018; 374: 361–383. doi: [10.1016/j.jcp.2018.07.033](https://doi.org/10.1016/j.jcp.2018.07.033)
- [21] Borazjani I, Ge L, Sotiropoulos F. Curvilinear immersed boundary method for simulating fluid structure interaction with complex 3D rigid bodies. *Journal of Computational Physics* 2008; 227(16): 7587–7620. doi: [10.1016/j.jcp.2008.04.028](https://doi.org/10.1016/j.jcp.2008.04.028)
- [22] Borazjani I, Ge L, Le T, Sotiropoulos F. A parallel overset-curvilinear-immersed boundary framework for simulating complex 3D incompressible flows. *Computers & Fluids* 2013; 77(Supplement C): 76–96. doi: [10.1016/j.compfluid.2013.02.017](https://doi.org/10.1016/j.compfluid.2013.02.017)
- [23] Borazjani I. Fluid–structure interaction, immersed boundary-finite element method simulations of bio-prosthetic heart valves. *Computer Methods in Applied Mechanics and Engineering* 2013; 257: 103–116. doi: [10.1016/j.cma.2013.01.010](https://doi.org/10.1016/j.cma.2013.01.010)
- [24] Luo K, Zhuang Z, Fan J, Haugen NEL. A ghost-cell immersed boundary method for simulations of heat transfer in compressible flows under different boundary conditions. *International Journal of Heat and Mass Transfer* 2016; 92: 708–717. doi: [10.1016/j.ijheatmasstransfer.2015.09.024](https://doi.org/10.1016/j.ijheatmasstransfer.2015.09.024)
- [25] Takahashi S, Nonomura T, Fukuda K. A Numerical Scheme Based on an Immersed Boundary Method for Compressible Turbulent Flows with Shocks: Application to Two-Dimensional Flows around Cylinders. *Journal of Applied Mathematics* 2014; 2014: 1–21. doi: [10.1155/2014/252478](https://doi.org/10.1155/2014/252478)
- [26] Seo JH, Mittal R. A sharp-interface immersed boundary method with improved mass conservation and reduced spurious pressure oscillations. *Journal of Computational Physics* 2011; 230(19): 7347–7363. doi: [10.1016/j.jcp.2011.06.003](https://doi.org/10.1016/j.jcp.2011.06.003)
- [27] Pasquariello V, Hammerl G, Örley F, et al. A cut-cell finite volume – finite element coupling approach for fluid–structure interaction in compressible flow. *Journal of Computational Physics* 2016; 307: 670–695. doi: [10.1016/j.jcp.2015.12.013](https://doi.org/10.1016/j.jcp.2015.12.013)
- [28] Municchi F, Radl S. Consistent closures for Euler-Lagrange models of bi-disperse gas-particle suspensions derived from particle-resolved direct numerical simulations. *International Journal of Heat and Mass Transfer* 2017; 111: 171–190. doi: [10.1016/j.ijheatmasstransfer.2017.03.122](https://doi.org/10.1016/j.ijheatmasstransfer.2017.03.122)

- [29] Municchi F, Radl S. Momentum, heat and mass transfer simulations of bounded dense mono-dispersed gas-particle systems. *International Journal of Heat and Mass Transfer* 2018; 120: 1146–1161. doi: [10.1016/j.ijheatmasstransfer.2017.12.105](https://doi.org/10.1016/j.ijheatmasstransfer.2017.12.105)
- [30] Cristallo A, Verzicco R. Combined Immersed Boundary/Large-Eddy-Simulations of Incompressible Three Dimensional Complex Flows. *Flow, Turbulence and Combustion* 2006; 77(1-4): 3. doi: [10.1007/s10494-006-9034-6](https://doi.org/10.1007/s10494-006-9034-6)
- [31] Arienti M, Sussman M. An embedded level set method for sharp-interface multiphase simulations of Diesel injectors. *International Journal of Multiphase Flow* 2014; 59: 1–14. doi: [10.1016/j.ijmultiphaseflow.2013.10.005](https://doi.org/10.1016/j.ijmultiphaseflow.2013.10.005)
- [32] Battistoni M, Xue Q, Som S, Pomraning E. Effect of Off-Axis Needle Motion on Internal Nozzle and Near Exit Flow in a Multi-Hole Diesel Injector. *SAE International Journal of Fuels and Lubricants* 2014; 7(1): 167–182.
- [33] Zhao H, Quan S, Dai M, et al. Validation of a Three-Dimensional Internal Nozzle Flow Model Including Automatic Mesh Generation and Cavitation Effects. *Journal of Engineering for Gas Turbines and Power* 2014; 136(9). 092603doi: [10.1115/1.4027193](https://doi.org/10.1115/1.4027193)
- [34] Örley F, Hickel S, Schmidt SJ, Adams NA. Large-Eddy Simulation of turbulent, cavitating fuel flow inside a 9-hole Diesel injector including needle movement. *International Journal of Engine Research* 2017; 18(3): 195–211. doi: [10.1177/1468087416643901](https://doi.org/10.1177/1468087416643901)
- [35] Örley F, Pasquariello V, Hickel S, Adams NA. Cut-element based immersed boundary method for moving geometries in compressible liquid flows with cavitation. *Journal of Computational Physics* 2015; 283: 1–22. doi: [10.1016/j.jcp.2014.11.028](https://doi.org/10.1016/j.jcp.2014.11.028)
- [36] Örley F, Hickel S, Schmidt SJ, Adams NA. LES of cavitating flow inside a Diesel injector including dynamic needle movement. *Journal of Physics: Conference Series* 2015; 656: 012097. doi: [10.1088/1742-6596/656/1/012097](https://doi.org/10.1088/1742-6596/656/1/012097)
- [37] Huang C, Huang J, Wang Y, Xu C. Cloud cavitating flow around an axisymmetric projectile in the shallow water. In: ; 2018.
- [38] Park S, Seo J, Rhee SH, Lee S. 6DOF motion and Cavity Dynamics of a Ventilated Super-cavitating Vehicle with Control Fins. In: ASME Press. 2018
- [39] Xu C, Wang wY, Huang gC, Huang J, Yu C. The effect of free surface on cloud cavitating flow around a blunt body. *Journal of Hydrodynamics, Ser. B* 2017; 29(6): 979–986.
- [40] Xu C, Wang Y, Huang C, Yu C, Huang J. Analysis of Near-wall effect on cloud cavitating flow that surrounds an axisymmetric projectile using large eddy simulation with Cartesian cut-cell mesh method. *European Journal of Mechanics - B/Fluids* 2018; 67: 15–24. doi: [10.1016/j.euromechflu.2017.07.001](https://doi.org/10.1016/j.euromechflu.2017.07.001)
- [41] Gavaises M, Murali-Girija M, Rodriguez C, Koukouvinis P, Gold M, Pearson R. Numerical simulation of fuel dribbling and nozzle wall wetting. *International Journal of Engine Research* 0; 0(0): 1468087420985189. doi: [10.1177/1468087420985189](https://doi.org/10.1177/1468087420985189)
- [42] Berger M. Chapter 1 - Cut Cells: Meshes and Solvers. In: Abgrall R, Shu CW., eds. *Handbook of Numerical Methods for Hyperbolic Problems Applied and Modern Issues*. 18 of *Handbook of Numerical Analysis*. Elsevier. 2017 (pp. 1–22)
- [43] Hartmann D, Meinke M, Schröder W. A strictly conservative Cartesian cut-cell method for compressible viscous flows on adaptive grids. *Computer Methods in Applied Mechanics and Engineering* 2011; 200(9): 1038–1052. doi: [10.1016/j.cma.2010.05.015](https://doi.org/10.1016/j.cma.2010.05.015)
- [44] Schneiders L, Hartmann D, Meinke M, Schröder W. An accurate moving boundary formulation in cut-cell methods. *Journal of Computational Physics* 2013; 235: 786–809. doi: [10.1016/j.jcp.2012.09.038](https://doi.org/10.1016/j.jcp.2012.09.038)
- [45] Meinke M, Schneiders L, Günther C, Schröder W. A cut-cell method for sharp moving boundaries in Cartesian grids. *Computers & Fluids* 2013; 85: 135–142. International Workshop on Future of {CFD} and Aerospace Sciencesdoi: [10.1016/j.compfluid.2012.11.010](https://doi.org/10.1016/j.compfluid.2012.11.010)
- [46] Foundation TO. OpenFOAM. <http://www.openfoam.org/>; .
- [47] Hejranfar K, Ezzatneshan E, Fattah-Hesari K. A comparative study of two cavitation modeling strategies for simulation of inviscid cavitating flows. *Ocean Engineering* 2015; 108: 257 - 275. doi: <https://doi.org/10.1016/j.oceaneng.2015.07.016>
- [48] Ducoin A, Huang B, Young YL. Numerical Modeling of Unsteady Cavitating Flows around a Stationary Hydrofoil. *International Journal of Rotating Machinery* 2012. Copyright - Copyright © 2012 Antoine Ducoin et al. Antoine Ducoin et al. This is an open access article distributed under the Creative Commons Attribution License, which permits unrestricted use, distribution, and reproduction in any medium, provided the original work is properly cited; Last updated - 2015-04-15.

- [49] Leroux JB, Coutier-Delgosha O, Astolfi JA. A joint experimental and numerical study of mechanisms associated to instability of partial cavitation on two-dimensional hydrofoil. *Physics of fluids* 2005; 17(5): 052101.
- [50] Giannadakis E, Gavaises M, Arcoumanis C. Modelling of cavitation in diesel injector nozzles. *Journal of Fluid Mechanics* 2008; 616: 153–193. doi: [10.1017/S0022112008003777](https://doi.org/10.1017/S0022112008003777)
- [51] Koukouvinis P, Naseri H, Gavaises M. Performance of turbulence and cavitation models in prediction of incipient and developed cavitation. *International Journal of Engine Research* 2017; 18(4): 333–350. doi: [10.1177/1468087416658604](https://doi.org/10.1177/1468087416658604)
- [52] Holzmann T. *Mathematics, numerics, derivations and OpenFOAM®*. 2017
- [53] Issa R. Solution of the implicitly discretised fluid flow equations by operator-splitting. *Journal of Computational Physics* 1986; 62(1): 40–65. doi: [10.1016/0021-9991\(86\)90099-9](https://doi.org/10.1016/0021-9991(86)90099-9)
- [54] Patankar S, Spalding D. A calculation procedure for heat, mass and momentum transfer in three-dimensional parabolic flows. *International Journal of Heat and Mass Transfer* 1972; 15(10): 1787–1806. doi: [10.1016/0017-9310\(72\)90054-3](https://doi.org/10.1016/0017-9310(72)90054-3)
- [55] Nikolaos Kyriazis and Phoevos Koukouvinis and Manolis Gavaises . Modelling cavitation during drop impact on solid surfaces. *Advances in Colloid and Interface Science* 2018. doi: [10.1016/j.cis.2018.08.004](https://doi.org/10.1016/j.cis.2018.08.004)
- [56] Schmidt S, Sezal I, Schnerr G, Talhamer M. Riemann techniques for the simulation of compressible liquid flows with phase-transition at all Mach numbers-shock and wave dynamics in cavitating 3-D micro and macro systems. In: ; 2008: 1238.
- [57] Moukalled F, Mangani L, Darwish M, others . *The Finite Volume Method in Computational Fluid Dynamics: An Advanced Introduction with OpenFOAM® and Matlab*. Springer . 2016.
- [58] Blazek J. *Computational fluid dynamics: principles and applications*. Butterworth-Heinemann . 2015.
- [59] Balaras E. Modeling complex boundaries using an external force field on fixed Cartesian grids in large-eddy simulations. *Computers & Fluids* 2004; 33(3): 375–404. doi: [10.1016/S0045-7930\(03\)00058-6](https://doi.org/10.1016/S0045-7930(03)00058-6)
- [60] Fortes-Patella R, Coutier-Delgosha O, Reboud J. Evaluation of the turbulence model influence on the numerical simulations of unsteady cavitation. *J. Fluids Eng* 2003; 125(1): 38–45.
- [61] Coutier-Delgosha O, Fortes-Patella R, Reboud JL. Simulation of unsteady cavitation with a two-equation turbulence model including compressibility effects. *Journal of Turbulence* 2002; 3: N58. doi: [10.1088/1468-5248/3/1/058](https://doi.org/10.1088/1468-5248/3/1/058)
- [62] Reboud JL, Stutz B, Coutier O. Two phase flow structure of cavitation: experiment and modeling of unsteady effects. In: ; 1998.
- [63] Menter FR. Two-equation eddy-viscosity turbulence models for engineering applications. *AIAA journal* 1994; 32(8): 1598–1605. doi: [10.2514/3.12149](https://doi.org/10.2514/3.12149)
- [64] NASA LRC. Turbulence Modeling Resource. <https://turbmodels.larc.nasa.gov//>; .
- [65] Wilcox DC, others . *Turbulence modeling for CFD*. 2. DCW industries La Canada, CA . 1998.
- [66] Dütsch H, Durst F, Becker S, Lienhart H. Low-Reynolds-number flow around an oscillating circular cylinder at low Keulegan–Carpenter numbers. *Journal of Fluid Mechanics* 1998; 360: 249–271. doi: [10.1017/S002211209800860X](https://doi.org/10.1017/S002211209800860X)
- [67] OpenCFD . OpenFOAM+. <http://www.openfoam.com/>; .
- [68] Hurlbut SE, Spaulding ML, White FM. Numerical Solution for Laminar Two Dimensional Flow About a Cylinder Oscillating in a Uniform Stream. *Journal of Fluids Engineering* 1982; 104(2): 214–220.
- [69] Sun Y, Shu C, Wang Y, Teo C, Chen Z. An immersed boundary-gas kinetic flux solver for simulation of incompressible flows. *Computers & Fluids* 2017; 142: 45–56. Selected papers of 18th International Conference on Finite Elements in Flow Problems doi: [10.1016/j.compfluid.2016.01.007](https://doi.org/10.1016/j.compfluid.2016.01.007)
- [70] Silva ALE, Silveira-Neto A, Damasceno J. Numerical simulation of two-dimensional flows over a circular cylinder using the immersed boundary method. *Journal of Computational Physics* 2003; 189(2): 351–370. doi: [10.1016/S0021-9991\(03\)00214-6](https://doi.org/10.1016/S0021-9991(03)00214-6)
- [71] Palma PD, Tullio dM, Pascazio G, Napolitano M. An immersed-boundary method for compressible viscous flows. *Computers & Fluids* 2006; 35(7): 693–702. Special Issue Dedicated to Professor Stanley G. Rubin on the Occasion of his 65th Birthday doi: [10.1016/j.compfluid.2006.01.004](https://doi.org/10.1016/j.compfluid.2006.01.004)
- [72] Kim J, Kline SJ, Johnston JP. Investigation of a Reattaching Turbulent Shear Layer: Flow Over a Backward-Facing Step. *Journal of Fluids Engineering* 1980; 102(3): 302–308. doi: [10.1115/1.3240686](https://doi.org/10.1115/1.3240686)

- [73] Hackman LP, Raithby GD, Strong AB. Numerical predictions of flows over backward-facing steps. *International Journal for Numerical Methods in Fluids* 1984; 4(8): 711–724. doi: [10.1002/fld.1650040802](https://doi.org/10.1002/fld.1650040802)
- [74] Armaly BF, Durst F, Pereira JCF, Schönung B. Experimental and theoretical investigation of backward-facing step flow. *Journal of Fluid Mechanics* 1983; 127: 473–496. doi: [10.1017/S0022112083002839](https://doi.org/10.1017/S0022112083002839)
- [75] Le H, Moin P, Kim J. Direct numerical simulation of turbulent flow over a backward-facing step. *Journal of Fluid Mechanics* 1997; 330: 349–374. doi: [10.1017/S0022112096003941](https://doi.org/10.1017/S0022112096003941)
- [76] BILLIG FS. Shock-wave shapes around spherical-and cylindrical-nosed bodies.. *Journal of Spacecraft and Rockets* 1967; 4(6): 822-823. doi: [10.2514/3.28969](https://doi.org/10.2514/3.28969)
- [77] Modesto-Madera NA. A Numerical Study of Supersonic Flow past a Circular Cylinder. Master Thesis; 2010.
- [78] Farrell P, Maddison J. Conservative interpolation between volume meshes by local Galerkin projection. *Computer Methods in Applied Mechanics and Engineering* 2011; 200(1): 89–100. doi: [10.1016/j.cma.2010.07.015](https://doi.org/10.1016/j.cma.2010.07.015)
- [79] Dular M, Coutier-Delgosha O. Numerical modelling of cavitation erosion. *International journal for numerical methods in Fluids* 2009; 61(12): 1388–1410.
- [80] Leroux JB, Astolfi JA, Billard JY. An experimental study of unsteady partial cavitation. *Journal of fluids engineering* 2004; 126(1): 94–101.
- [81] Menter FR, Langtry R, Völker S. Transition Modelling for General Purpose CFD Codes. *Flow, Turbulence and Combustion* 2006; 77(1): 277–303. doi: [10.1007/s10494-006-9047-1](https://doi.org/10.1007/s10494-006-9047-1)
- [82] Gomez Santos E, Shi J, Gavaises M, Soteriou C, Winterbourn M, Bauer W. Investigation of cavitation and air entrainment during pilot injection in real-size multi-hole diesel nozzles. *Fuel* 2020; 263: 116746. doi: <https://doi.org/10.1016/j.fuel.2019.116746>
- [83] Kolovos K, Koukouvinis P, McDavid RM, Gavaises M. Transient Cavitation and Friction-Induced Heating Effects of Diesel Fuel during the Needle Valve Early Opening Stages for Discharge Pressures up to 450 MPa. *Energies* 2021; 14(10). doi: [10.3390/en14102923](https://doi.org/10.3390/en14102923)
- [84] Vidal A, Kolovos K, Gold MR, Pearson RJ, Koukouvinis P, Gavaises M. Preferential cavitation and friction-induced heating of multi-component Diesel fuel surrogates up to 450MPa. *International Journal of Heat and Mass Transfer* 2021; 166: 120744. doi: <https://doi.org/10.1016/j.ijheatmasstransfer.2020.120744>
- [85] Strotos G, Koukouvinis P, Theodorakakos A, et al. Fuel heating in high pressure diesel nozzles. *Thiesel, Valencia, Spain* 2014.
- [86] Egerer CP, Hickel S, Schmidt SJ, Adams NA. Large-eddy simulation of turbulent cavitating flow in a micro channel. *Physics of Fluids* 2014; 26(8): 085102. doi: [10.1063/1.4891325](https://doi.org/10.1063/1.4891325)
- [87] Cristofaro M, Edelbauer W, Gavaises M, Koukouvinis P. Numerical simulation of compressible cavitating two-phase flows with a pressure-based solver. In: ; 2017. This work is licensed under a Creative Commons 4.0 International License (CC BY-NC-ND 4.0).
- [88] Cristofaro M, Edelbauer W, Koukouvinis P, Gavaises M. Influence of Diesel Fuel Viscosity on Cavitating Throttle Flow Simulations under Erosive Operation Conditions. *ACS Omega* 2020; 5(13): 7182-7192. doi: [10.1021/acsomega.9b03623](https://doi.org/10.1021/acsomega.9b03623)
- [89] Bergeles G, Li J, Wang L, Koukouvinis F, Gavaises M. An Erosion Aggressiveness Index (EAI) Based on Pressure Load Estimation Due to Bubble Collapse in Cavitating Flows Within the RANS Solvers. *SAE International Journal of Engines* 2015; 8(5): 2276–2284.
- [90] Koukouvinis P, Karathanassis IK, Gavaises M. Prediction of cavitation and induced erosion inside a high-pressure fuel pump. *International Journal of Engine Research* 2018; 19(3): 360-373. doi: [10.1177/1468087417708137](https://doi.org/10.1177/1468087417708137)
- [91] Lemmon E, Huber M, McLinden M. NIST Standard Reference Database 23: Reference Fluid Thermodynamic and Transport Properties-REFPROP, Version 8.0. 2007.
- [92] Nicoud F, Ducros F. Subgrid-scale stress modelling based on the square of the velocity gradient tensor. *Flow, turbulence and Combustion* 1999; 62(3): 183–200. doi: [10.1023/A:1009995426001](https://doi.org/10.1023/A:1009995426001)
- [93] Mitroglou N, McLorn M, Gavaises M, Soteriou C, Winterbourne M. Instantaneous and ensemble average cavitation structures in Diesel micro-channel flow orifices. *Fuel* 2014; 116: 736-742. doi: [10.1016/j.fuel.2013.08.060](https://doi.org/10.1016/j.fuel.2013.08.060)